Dissertation

Imaging as Characterization Techniques for Thin-Film Cadmium Telluride Photovoltaics

Submitted by

Katherine Zaunbrecher

Department of Physics

In partial fulfillment of the requirements

For the Degree of Doctor of Philosophy

Colorado State University

Fort Collins, Colorado

Spring 2014

Doctoral Committee:

Advisor: James R. Sites

Martin Gelfand
Kristen Buchanan
W.S. Sampath

Abstract

Imaging as Characterization Techniques for Thin-Film Cadmium Telluride Photovoltaics

The goal of increasing the efficiency of solar cell devices is a universal one. Increased photovoltaic (PV) performance means an increase in competition with other energy technologies. One way to improve PV technologies is to develop rapid, accurate characterization tools for quality control. Imaging techniques developed over the past decade are beginning to fill that role.

Electroluminescence (EL), photoluminescence (PL), and lock-in thermography are three types of imaging implemented in this study to provide a multifaceted approach to studying imaging as applied to thin-film CdTe solar cells. Images provide spatial information about cell operation, which in turn can be used to identify defects that limit performance.

This study began with developing EL, PL, and dark lock-in thermography (DLIT) for CdTe. Once imaging data were acquired, luminescence and thermography signatures of non-uniformities that disrupt the generation and collection of carriers were identified and catalogued. Additional data acquisition and analysis were used to determine luminescence response to varying operating conditions. This includes acquiring spectral data, varying excitation conditions, and correlating luminescence to device performance.

EL measurements show variations in a cell's local voltage, which include inhomogeneities in the transparent-conductive oxide (TCO) front contact, CdS window layer, and CdTe absorber layer. EL signatures include large gradients, local reduction of luminescence, and local increases in luminescence on the interior of the device as well as bright spots located

on the cell edges. The voltage bias and spectral response were analyzed to determine the response of these non-uniformities and surrounding areas.

PL images of CdTe have not shown the same level of detail and features compared to their EL counterparts. Many of the signatures arise from reflections and severe inhomogeneities, but the technique is limited by the external illumination source used to excite carriers. Measurements on unfinished CdS and CdTe films reveal changes in signal after post-deposition processing treatments.

DLIT images contained heat signatures arising from defect-related current crowding. Forward- and reverse-bias measurements revealed hot spots related to shunt and weak-diode defects. Modeling and previous studies done on Cu(In,Ga)Se_2 thin-film solar cells aided in identifying the physical causes of these thermographic and luminescence signatures. Imaging data were also coupled with other characterization techniques to provide a more comprehensive examination of nonuniform features and their origins and effects on device performance. These techniques included light-beam-induced-current (LBIC) measurements, which provide spatial quantum efficiency maps of the cell at varying resolutions, as well as time-resolved photoluminescence and spectral PL mapping. Local drops in quantum efficiency seen in LBIC typically corresponded with reductions in EL signal while minority-carrier lifetime values acquired by time-resolved PL measurements correlate with PL intensity.

Acknowledgements

I will forever be indebted to my Society of Physics Students friends. Your enthusiasm and support has done so much to encourage me. For my University of Louisiana physics family – I am not sure that I would have come so far without your support and love. You have taught me so much. I am grateful for my friends and colleagues at CSU, who have helped me through classes, research, and so much more. I am especially appreciative of my advisor, Jim, who has helped me grow as a researcher. To my family, who has provided so much from the very beginning – I hope that I have shown you the same support and love that you have given to me. To my first mentor, Dr. Meriwether, Pa – thank you for encouraging me to grow while fostering my curiosity. And for Douglas, who chose to accompany me on my adventure. Thank you for believing in me, pushing me, and being on my team.

This dissertation is dedicated to my friend Richard Painter.

Table of Contents

CHAPTER 1

Introduction

1.1. Why Photovoltaics?

Oil and coal, humans' two major sources of energy on Earth, are finite resources. Because of the present non-urgency of this fact, the importance of alternative energy, and specifically renewable energy, is not yet realized by all. Yet research in renewable technologies, especially photovoltaics, is continuing to expand in the U.S. and around the world. Photovoltaic technology has advanced considerably in the past decade. The devices themselves are becoming more efficient and the cost is dropping significantly (although the up-front cost for installation is still very high). New cost goals are as low as $1/Watt installed.

Silicon solar cells were first manufactured for commercial use in the late 1950's in the U.S. New materials for photovoltaic devices made their debut in the 1980's. Today, solar cells have reached a level of sophistication that would allow enough PV energy production to power the entire U.S. The photovoltaic effect, the concept of taking energy from the sun and converting it into electrical energy, is simple. The physics behind this process is explained in the next section. The scope of this project includes applying this physics to photovoltaic characterization techniques to determine what limits PV device efficiency. Specific focus is on developing imaging techniques that produce rapid, qualitative spatial information.

1.2. Physics of Photovoltaics

A solar cell, at first glance, is a straightforward device. On its most basic level, it creates a current via the photoelectric effect. Incident photons from the sun are absorbed by the solar cell, the energy from these photons is used to create electron-hole pairs (charged carriers),

and the carriers are then collected in an external circuit. Solar cells are typically made of semiconductor materials. A standard device consists of an n-type and a p-type material brought together to form a p-n heterojunction diode. There are conductive materials placed on either side of the p-n sandwich to carry the generated electrons and holes to an external circuit to generate electricity. Because a solar cell behaves like a semiconductor diode, which allows current to easily flow in one direction through the junction and prohibits current flow in the other, the standard diode equation can be used to characterize photovoltaic devices:

$$J = J_o e^{\frac{q}{Ak_BT}(V-JR)} + GV - J_L. \tag{1}$$

Here, J_o is the dark saturation current (or forward current), q is electronic charge, A is the dimensionless diode quality factor, k_B is Boltzman's constant, T is temperature, V is voltage, and J_L is the light-generated photocurrent. Losses due to resistances, in the form of series resistances, R, and shunt conductance, G, are also factored in. This equation is derived from Poisson's equation, which relates the charge and electric field strength, the transport equation to describe the flow of carriers, and the continuity equations, which describe carrier movement, generation, and recombination [1].

When a cell is in thermal equilibrium, there is no generation of excess carriers. During illumination or when a bias is placed on the cell, electron-hole pairs are generated and either collected by an external circuit or recombine. These carriers have an average lifetime characterized by the time it takes for recombination to occur. There is also a diffusion length denoting the average distance the carriers move through the device before recombining.

The p-n junction is where much of the carrier generation occurs. This is good for the current collection, because the asymmetry of the junction forms a depletion region that has

a built-in electric field. Any electrons and holes that are formed inside of or move into the depletion region are carried by the electric field to opposite ends of the device, where they get collected as current, provided they do not recombine first. Recombination mechanisms include radiative recombination, where the electron-hole pair emit a photon, and Shockley-Read-Hall recombination due to deep-level states between the conduction and valence bands.

Ideally, every incident photon of sufficient energy would create an electron-hole pair that is collected by the external circuit. But there are limitations due to optical and electronic losses (including minority-carrier lifetime and diffusion length) which lower the collection efficiency. In order to understand these losses and how to minimize them, one must first look at the properties of each layer, how photons and carriers move through these layers, and how the device as a whole functions.

1.2.1. Cell Geometry. Solar cell devices typically consist of a back electrical contact (usually metal), a p-type absorber material, an n-type window layer, and a transparent conducting oxide (TCO) layer for the front contact. Cells are connected in series to form a module, which is placed between two pieces of glass and then sealed. The quality and composition of the front glass is such to minimize reflection and increase absorption of sunlight. The TCO is electrically conductive to allow for the transport of carriers but, similar to the glass, optically transparent for transmission of incident photons.

The p-type absorber layer in a solar cell is named such because the majority of its carriers are holes rather than electrons. This is also where most of the carrier collection, or photon absorption, takes place. The n-type material contains more electrons than holes and is called the window layer because the majority of photons incident on the device pass through this layer and get absorbed in the p-type layer, as the band gap energy of the n-type material

is higher than the energy of most of the incident photons. In order for a photon to excite an electron-hole pair it must have enough energy to span the band gap, or energy difference between the valence and conduction bands of the material.

Despite the simple geometry of solar cells, the electronic and optical properties of the materials can greatly affect the efficiency of the device. When lower-cost polycrystalline materials are used, the morphology of the grains of the window and absorber layers, including grain size and grain boundaries, as well as the interfaces between the layers, affect the movement of the carriers throughout the cell. Impurities in the materials, voids, and other defect and trapping states (which are explained in more detail below) will also lead to greater recombination and less current collection.

1.2.2. Characterizing Solar Cell Performance. Photovoltaic device performance is characterized by a series of parameters, including cell efficiency, open-circuit voltage, short-circuit current density, and the maximum power point. Standard measurements to extract these parameters include current density-voltage, or J-V, measurements. J-V data are acquired by sweeping a voltage bias across a cell and measuring the current output in both light and dark conditions. When looking at J-V data, one expects the dark curve to be a standard diode curve, with very small current density values at lower voltages and a rapid increase in current at the turn-on voltage. An example of J-V curves is shown in Fig. 1.1.

Performance parameters such as V_{OC}, J_{SC}, and η are extracted from the data. The short-circuit current density (J_{SC}) is the current density through the illuminated cell when the voltage across the cell is zero. Open-circuit voltage (V_{OC}) refers to the voltage of the device when the current through the illuminated cell is zero. Each cell has a maximum power point (with corresponding maximum current density and voltages under illumination), and

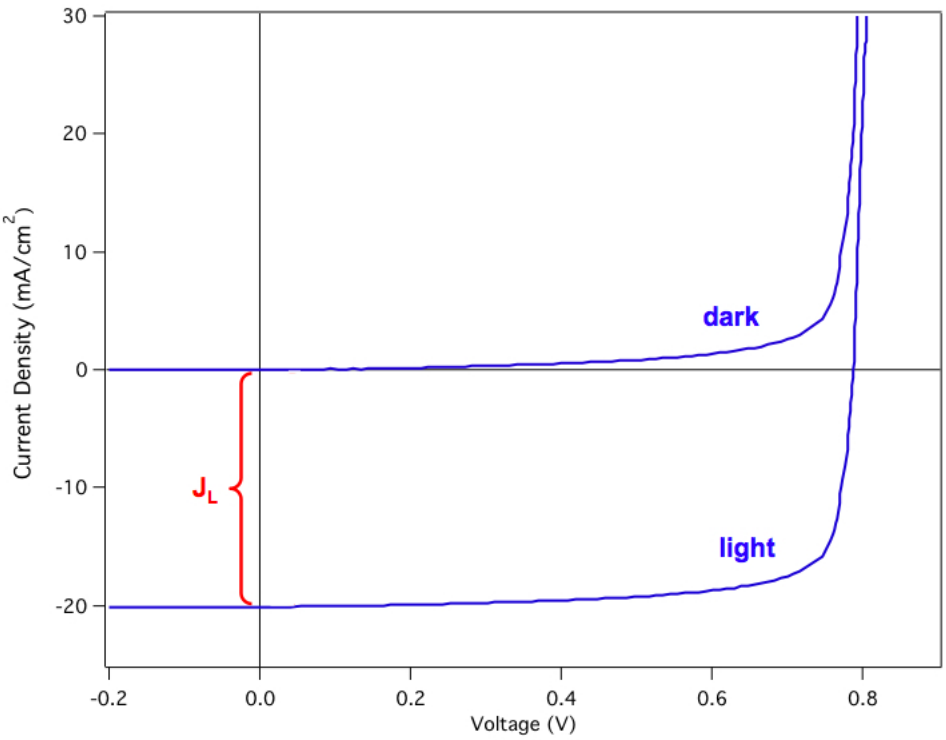

FIGURE 1.1. Dark and light J-V curves taken from a well-behaved solar cell. J_{SC} and V_{OC} values are extracted from the light curve.

a fill factor (FF), which describes the maximum power that can be extracted from the cell. The fill factor is given by the ratio of the maximum current and voltage to the short-circuit current density and open-circuit voltage,

$$FF = \frac{J_{MP}V_{MP}}{J_{SC}V_{OC}}. \tag{2}$$

Efficiency, denoted as η, is the major characterization parameter. It is the ratio of generated power to the incident power and is given by,

$$\eta = \frac{V_{OC}J_{SC}FF}{P_{in}}. \tag{3}$$

Quantum efficiency, or QE, varies with wavelength and is the probability for one incident photon to generate one electron to the external circuit. QE measurements monitor the

current output of each cell as a function of wavelength. This involves directing a light beam onto the surface of a cell and measuring the current that is generated as the wavelengths of the light is swept over an appropriate range. Other characterization techniques such as capacitance-voltage (C-V) help determine carrier concentrations and doping levels while optical measurements such as reflection and transmission determine the number of incident photons reflected by and transmitted through the front glass and contacts. The J-V, QE, C-V, and reflectance measurements are used in the CSU Photovoltaics Laboratory.

The two types of resistance introduced in the diode equation, series resistance and shunt resistance, are detrimental to solar cell performance. Series resistance comes from resistance to current flow, usually through the front and back contacts. Shunt resistance comes from leakage current across the cell where power is dissipated. It redirects the current through the cell into the defect region and decreases the amount flowing through the unaffected areas, ultimately dropping the cell's voltage. It is a result of the manufacturing process and typically arises when there are weak or thin layers of the p-n junction so that a highly conductive path is created between the two contacts. Weak diodes are areas that are compromised by a reduced turn-on voltage. There is also resistance in the TCO layer, called sheet resistance, which limits the lateral current flow through the device. Other areas of high resistance, delamination, and mid-band-gap traps are other types of common defects found in PV devices.

1.2.3. Thin-film Photovoltaics. Thin-film photovoltaics require only a thin layer of a semiconductor absorber material with a high absorption coefficient. Cadmium telluride (CdTe), copper indium gallium disellinium ($Cu(In,Ga)Se_2$, or CIGS), and amorphous silicon (a-Si) devices are the three most common types of thin-film solar cells. Thin-film devices must

use direct band gap materials, which means that the lowest energy in the conduction band lies directly above the point of highest energy in the valence band (on the energy-k wavevector plot). Direct band gaps are better for photon absorption and collection than their indirect gap counterparts, such as multicrystalline Si (mc-Si), because carrier generation takes place close to or in the junction and loss of carriers through recombination is reduced [2].

Thin-film cells are the focus in the PV laboratory at Colorado State University. The measurements described above are typically used to characterize device performance of CdTe and CIGS devices. Previous work has also included modeling thin-film devices, both on the cell and module levels. This study moves beyond modeling to acquire experimental results using different characterization tools. Through these measurements one can determine what is limiting cell efficiency and how to make improvements. This information can in turn be given to the manufacturers to produce better devices.

1.3. CdTe Solar Cells

The characterization of CdTe solar cells is a central part of this work. CdTe cells are most commonly superstrate devices, meaning that incident light first passes through glass before the front contact and top layers. Superstrate devices are made from top to bottom, starting with a top glass layer, adding the top-contact TCO, then the window and absorber layers, and finally the back contacts. CdTe has a band-gap energy of 1.47 eV and its absorption spectrum matches the sun's spectrum very well. The cost per watt is also competitively low, with prices now comparable to silicon solar cells. Module cost is as low as \$0.49/W with installation prices down to \$1.40/W.

The CdTe material used for the absorber layer is inherently p-type because of the presence of specific intrinsic defects. As a result, additional doping has been hard to achieve. Because

high doping is difficult to achieve, this limits carrier concentrations. Manufacturers must then turn to other avenues to increase the performance of CdTe cells. This includes post-CdTe-deposition treatments such as exposing the films to $CdCl_2$ at high temperatures, which appears to improve grain structure. Other post-deposition treatments include treating the film with copper and further annealing at high temperatures. These processing steps, among others, are used at CSU to fabricate lab-size CdTe solar cells, as explained below.

1.3.1. Colorado State University's CdTe Program. The CdTe solar cells used in this particular study were made at the Materials Engineering Laboratory at CSU. The individual cells were small-area devices delineated on a 3" × 3" glass substrate. Each substrate, which is acquired with the fluorine-doped SnO_2 front-contact layer (TCO) already deposited on it, runs through the deposition chamber of the Advanced Research and Development System (ARDS) at the Materials Engineering Laboratory. The ARDS uses heated-pocket deposition to deposit the material on the glass substrate. This technology, based on close-space sublimation (CSS), uses heated sources to evaporate the material onto the piece of glass that runs linearly through the system by means of a transfer arm. CdS and CdTe, the window and absorber materials, are deposited on the TCO/glass with standard thicknesses of 120 nm for CdS and around 2.2 μm for CdTe. The glass is about 3 mm thick and the TCO layer is 400 nm. The substrates undergo several treatments, including an application of a $CdCl_2$ haze, which is then stripped away. Two Cu treatments then follow, with the substrate being exposed to sublimated Cu at high temperatures. The $CdCl_2$ and Cu treatments modify the grain structure and improve cell performance. The films are then annealed at high temperatures. The sample emerges from the chamber as an unfinished film with CdTe grain sizes around 1 μm. A back metal contact (C and Ni paste) is then applied using a spray

on the film. Following the back contact deposition, a mask is pressed onto the substrate and the uncovered area is sand-blasted away, removing the metal, CdTe, and CdS layers to delineate individual cells. A schematic showing the cell layers are shown in Fig. 1.2. Nine finished cells remain on the substrate, each around 0.7 cm^2 in area, as seen in Fig. 1.3.

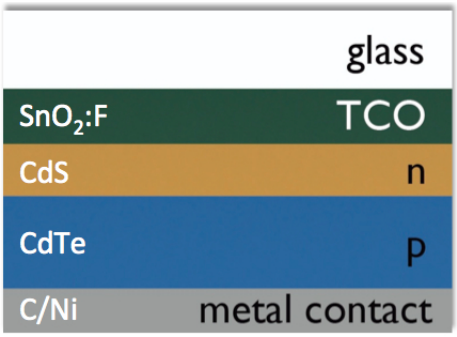

FIGURE 1.2. A simple schematic of a CdTe solar cell, not to scale. Typical thicknesses on CSU samples are 3 mm for the glass, 400 nm for TCO, 120 nm for CdS, 2.2 μm for CdTe, and about 1 mm for the back contact.

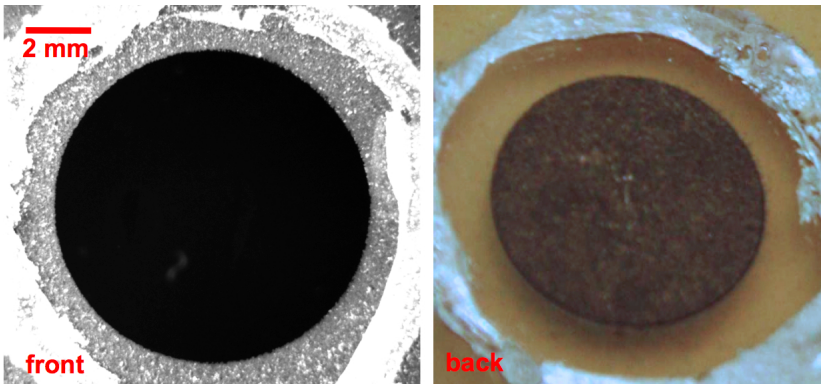

FIGURE 1.3. The front and back views of a CdTe solar cell made at CSU.

1.4. A Brief Introduction to Imaging

Multiple imaging techniques have been used to evaluate the quality of solar cells. The main advantage of imaging over other characterization techniques is its rapid speed, with images acquired in a matter of seconds. If employed in-line during the manufacturing process, it can prove to be helpful in quickly estimating photovoltaic performance.

Electroluminscence (EL) and photoluminescence (PL) are two imaging techniques that have become well established over the past decade as PV characterization tools. EL for PV was first implemented by a group in Japan who used it to image polycrystalline silicon devices [3], [4]. PL was established in Germany for PV applications, also on silicon solar cells [5], [6]. These measurements provide spatial information about current flow and carrier recombination in solar cells. Imaging has successfully led to the identification of defects in the cell, including shunts, changes in voltage across the cell, and non-uniform material deposition. Shunted areas in CIGS devices at the National Renewable Energy Laboratory (NREL) were identified using EL, PL, and lock-in thermography (LIT) [7]. Voltage drops across cells connected in series are seen in EL images of CIGS modules [8]. PL imaging of CIGS cells shows the uniformity and the electronic quality of the CIGS layer [7].

Most of the work on imaging has emphasized silicon devices. This study seeks to further develop imaging techniques as applied to thin-film devices, particularly CdTe. Initial studies on thin-film devices included modeling and imaging done on Cu(In,Ga)Se_2 devices [9], [10], the results of which were generalized for most other thin-film technologies. Before this study, there were few published results on imaging CdTe, and no imaging data acquired on CSU's CdTe devices. In the following chapters, imaging as an evaluation tool for CdTe is assessed. This work takes an extensive look at thin-film CdTe devices imaged using electroluminescence and photoluminescence imaging at NREL. It also examines how other imaging techniques and measurements are utilized to gain a better understanding of inhomogeneities that arise during manufacturing and how to make better devices.

CHAPTER 2

Electroluminescence Imaging

A p-n junction solar cell acts as a light-emitting diode in reverse. By placing a voltage across a solar cell, the solar cell will light up as a result of carriers being generated and recombining. Some of the recombining carriers emit a photon when the electron relaxes from the conduction band to the valence band, undergoing radiative recombination. EL imaging is the process of detecting these photons in order to provide a spatial map of this phenomenon. Acquisition and analysis of EL imaging data for CdTe solar cells are presented in this chapter.

The process of acquiring images is straightforward. The imaging system, as seen in Fig. 2.1, consists of a camera that sits above the sample that houses the detector which collects emitted photons. The data are then relayed to a computer and opened in an imaging software program. Interpretation of the data, on the other hand, requires analysis which is often times complex. Proper identification of defects and various efficiency-limiting effects is crucial, especially in providing rapid feedback to manufacturers in how to build better devices.

Data analysis involves several steps, beginning with parameterization, which includes assessing the overall uniformity of the cell. This means looking at each image and noting the amount and severity of variation in the EL signal, shown by a change in signal intensity. Distinct features or non-uniformities in the signal are then catalogued, including their shapes, sizes, and intensity signatures. Further data processing is done by creating intensity profiles around non-uniform features and comparison of the luminescence images with

other characterization data. This is an important step in imaging because it will eventually allow quantitative analysis of the images, which, in turn will allow for rapid in-line PV characterization.

Previous studies have used full panels, with many cells connected in series, in EL imaging [8], [9], producing images of entire modules (around 0.75-1 m^2). This study emphasizes luminescence images on the individual cell level for extensive exploration of small-area photovoltaic response. Focus will be on variations in EL signal due to cell type, quality, current through the cell, emission spectrum, and non-uniform features.

The data, taken at the National Renewable Energy Laboratory (NREL), allow for the spatial identification of inhomogeneities in solar cells. With the proper analysis the physical causes of these inhomogeneous features seen in imaging can be identified. Emphasis is placed on the use of EL imaging to characterize thin-film CdTe cells.

2.1. Experimental Setup

The setup for electroluminescence imaging at the NREL includes a cooled silicon charge-coupled device (CCD) camera with 1024×1024 pixels^2. It is a Princeton Instruments/Acton PIXIS back-reflector camera. It is housed in a light-tight enclosure, mounted on a track which can move the camera vertically. It sits above a translatable stage where the sample is placed. A full solar cell with front and back contacts is needed for EL measurements, as it must be connected to a power supply to be biased. The camera captures the light being emitted from the cell by recombination of charge carriers that are generated from the voltage bias. The camera is run by WinVue software, which compiles an image from the photons being captured by the Si detector inside the camera.

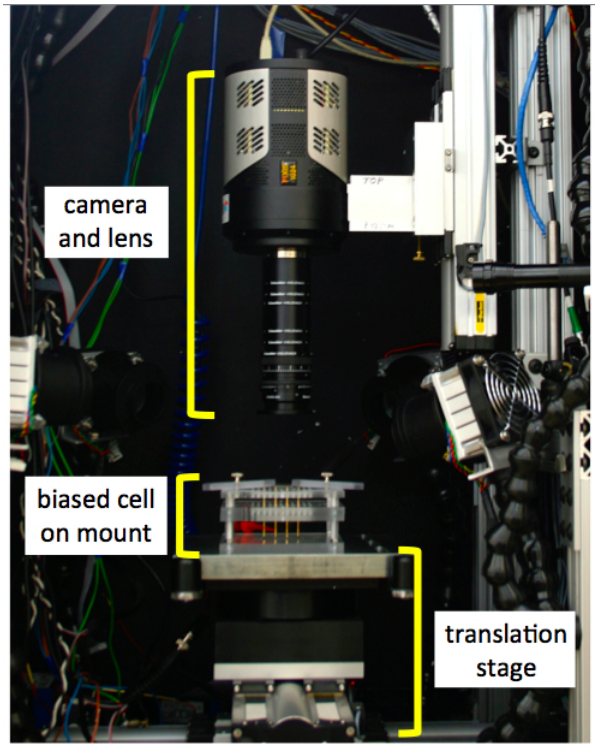

FIGURE 2.1. EL setup, including CCD camera, at NREL.

The response of the camera is highly dependent upon the quantum efficiency of the Si detector that sits inside of it. Its QE peaks between 750 and 800 nm at around 94%, as shown in Fig. 2.2. Values drop below 50% at wavelengths lower than 450 nm and higher than 950 nm. The focusing optics, made up of a lens and extension rings, limits the resolution. The standard lens that was used to image the 0.7 cm^2 CdTe samples had a maximum resolution of 6 μm/pixel. There is also a background signal from the camera, which was consistent with exposure time.

2.2. IMAGING DATA PROCESSING

WinVue provides an image whose intensity corresponds to the number of photons detected by each pixel and the QE of the camera. This intensity is displayed in arbitrary units as a grey scale. The exposure time is set by the user. Background images are taken before

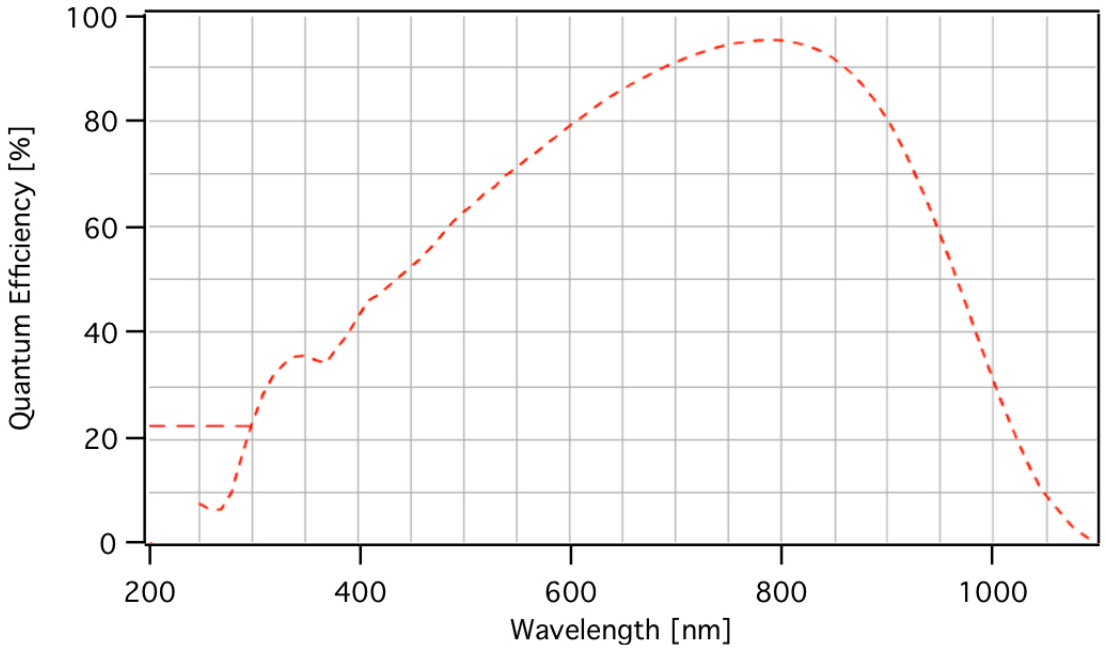

FIGURE 2.2. The quantum efficiency response of the Si CCD used in the camera for EL imaging as provided by the manufacturer.

each EL image to determine the background signal to be subtracted from images. A log scale is used to set voltage biases to achieve certain current densities for the measurements: 1, 2, 4, 10, 20, and 40 mA/cm^2. These values fall in the range of operation for solar cells. For 40 mA/cm^2, which is equivalent to almost twice the short-circuit current density, the poor devices are in danger of shorting and the voltage and current drifts. Also running the cell at J_{SC} or higher causes the cell to heat up substantially. Therefore the current-limiting mode on the power supply needs to be used to control the otherwise unstable current. So the typical maximum current density is 20 mA/cm^2.

Expectations can be formed based on previous studies on imaging, both on multicrystalline Si (mc-Si) and other thin-film technologies, and knowledge of device physics. The expectations for EL imaging on CdTe are as follows. When the current density, J, increases through the cell and approaches J_{SC}, the device heats up, performance decreases, and the luminescence signal decreases because there are less carriers being generated. The expected

maximum signal should have an energy at 1.47 eV, which corresponds to the band gap energy of CdTe. The limitations of EL imaging include the manifestation of R_S effects such as lateral variations in current due to series resistance, which complicate the quantitative interpretation of the images [5]. This complication arises because it is difficult to distinguish R_S variation from local increased carrier recombination when looking at contrast in EL signal. If any gaps in the material exist or electrical contact between the layers does not exist, this will keep current from flowing in that area and a signal will not be detected.

2.2.1. Calibrations. Camera calibrations were started in hopes of comparing EL images to data acquired with other cameras. Total quantification requires converting the signal to equivalent current units. The sample geometry, the geometry of the system, including sample, lens, and camera placement, the quantum efficiency of the camera, and losses due to reflection must all be considered.

The 1024 pixel $\times$ 1024 pixel detector in the camera transfers its signal in the form of a 16-bit image to the camera software. With the camera set to its standard acquisition speed of 2 MHz and the control at high gain, the given number of electrons per ADU (an arbitrary analog-to-digital unit), calibrated by the company, was 1.05. The ADU value is the intensity of signal for each pixel, which is shown as a greyscale in the image processing software. The pixel area of the selected region of the cell is determined and related to the physical area of that cell region to obtain a value for the number of pixels per area (in pixels/cm^2). Quantitative analysis must then fold in optical losses, exposure time, and noise.

An initial estimate of the photon flux (number photons emitted from the sample per square centimeter per second) can be calculated from the EL intensity and the area of the imaged region, taking into account mean pixel counts, the number of pixels contained in the

region of interest (ROI), the area of the ROI, and factoring in a 20% loss from the lenses:

$$J_{ph} = \frac{\text{average EL intensity} * 1.05 \text{ electron} * 0.8 \text{ photon/electron}}{\text{ROI area } [cm^2] * \text{exposure time } [s]}, \tag{4}$$

where 1.05 is the values for the electrons per ADU as taken from the specification provided by PIXIS. Even though this calculated value does not provide the external radiative efficiency typically calculated for luminescence data [11], this gives a good estimate of the radiative recombination so that comparisons can be made between samples.

The EL intensity, which is dependent upon lateral location in the cell, and hence the use of $\vec{r} = (x,y)$, can be expressed as

$$\phi_{EL}(E,\vec{r}) \;=\; QE_e(E,\vec{r})\;\phi_{bb}(E)\;e^{\frac{qV(\vec{r})}{kT}}, \tag{5}$$

where QE_e is the local external QE given by $QE_e = [1 - R(E,\vec{r})]\;QE_i(E,\vec{r})$ (R is the front surface reflectance and QE_i is the internal quantum efficiency) [9]. ϕ_{bb} is blackbody emissions given by

$$\phi_{bb}(E) = \frac{2\pi E^2/(h^3c^2)}{e^{E/kT} - 1}, \tag{6}$$

where kT/q is thermal voltage, $V(\vec{r})$ is the internal junction voltage, and E is photon energy [9]. According to this expression, EL signal depends upon the local voltage, so any variation in voltage will be reflected in the luminescence image. This will be used later on when identifying defects via inhomogeneous luminescence.

2.2.2. EL Images. Images of CdTe cells acquired on the NREL system show the 0.7 cm^2 circular devices spanning the length and width of the pixels. The circular cell is contrasted

against the glass and transparent conducting oxide (TCO) in the background. The active part of the cell luminescences when a sufficient voltage is placed across the cell, and the image shows the circular area "lit up" against the dark background. The image shows variations in the EL signal being emitted from the cell that include regions of decreased signal, changes in intensity across large regions, and areas of increased luminescence. Some of these features are local, which, when used in this study, means that the affected area is on the order of less than 10% of the total cell area. The cells made at CSU are on the order of 0.7 cm^2, so this means local features are under 7 mm in diameter.

EL data are collected in the form of a 16-bit image, with the camera setup and detector previously explained. Each pixel acquires an analog signal in the form of current, which is then converted to a digital signal. The signal is then transformed into an intensity value, with arbitrary units, which can be read from the image open in the software. The software used for this study was ImageJ, a free open source software similar to many other commercially available imaging software packages. When the raw data from the camera are opened in ImageJ, each of the pixels in the 1024×1024 array has an intensity which corresponds to the digital current output. The standard images are seen in greyscale, with intensity values spanning 0 to $2^{16} = 65{,}536$, which correspond to the number of bins in the 16-bit data. A brighter signal where more photons are detected is shown as being more white, with a lack of signal shown as black.

Examples of EL images of different solar cell technologies as seen in ImageJ can be seen in Fig. 2.3. These images were all taken with the Si CCD camera at NREL. The Si sample, which is a typical polycrystalline Si wafer, was from a company working in partnership with NREL. The CdTe cell was made at CSU, and the CIGS cell was fabricated at NREL. The Si

sample is larger (20 cm × 20 cm) than the other two, so the field of view is correspondingly larger. The Si resolution is approximately 5 pixels/mm, whereas the resolution for the smaller CIGS and CdTe samples (with a 3 mm × 5 mm rectangular shape and 9 mm circular diameter, respectively) is approximately 100 pixels/mm.

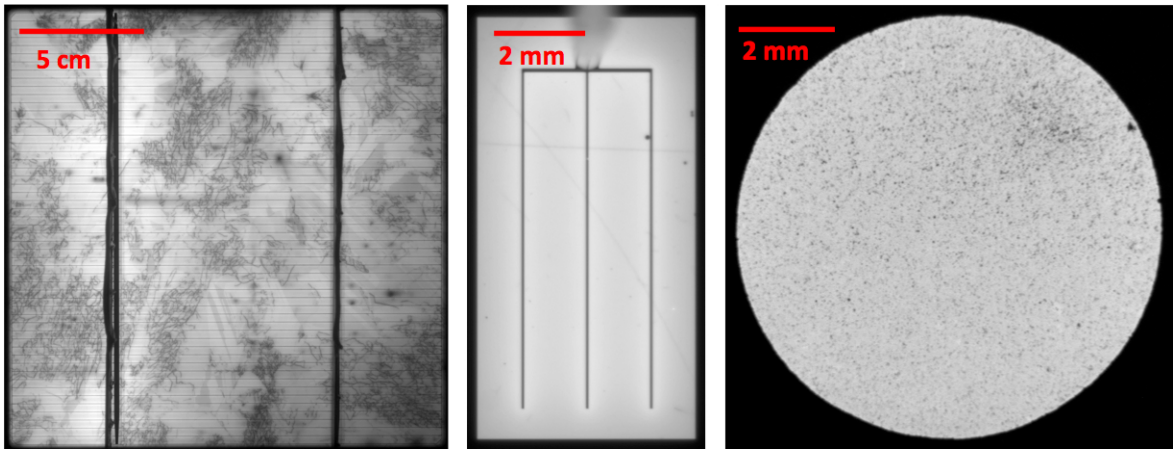

FIGURE 2.3. EL images of Si, CIGS, and CdTe solar cells viewed using Image J software. The color scale used is grayscale, going from black (no signal) to white (the most signal).

The wavelength response of the camera corresponds to the quantum efficiency (QE) response of the Si CCD detector provided by the manufacturer and seen in Fig. 2.2. The band gaps for the materials, however, vary. The Si sample has a band gap energy of 1.1 eV (corresponding to a wavelength of 1126 nm), so that the detector has a quantum efficiency of approximately 10% for its band-to-band emission. The band gap of the CIGS sample with 43% Ga is 1.3 eV (954 nm), which means that the camera is 60% responsive at the dominant band-to-band emissions. The CdTe solar cell has a band gap energy of 1.45 eV (855 nm), which corresponds to a 90% camera QE value. Despite the low-QE camera response for Si, a signal is still easily detected because of the high EL efficiency from Si cells.

The primary EL focus was on CdTe devices. Consistent conditions for these EL measurements included having standard values for current density and exposure times. Current

density values started at 2 mA/cm^2 and continued to 4, 10, and 20 mA/cm^2, with occasional measurements with 40 mA/cm^2 currents. 20 mA/cm^2, near the short-circuit current density (J_{SC}) for the CdTe samples, was adopted as the baseline. The baseline exposure time was set at 30 seconds. A background image with zero current through the cell was also taken before all measurements so that the background noise could be subtracted from the biased images to obtain a more accurate signal value.

2.2.3. Spectral Response of EL. A set of 5 different 50-mm-diameter round long-pass filters attached to the camera lens was used to acquire spectral information about the luminescence from CdTe cells. Nominal minimum wavelengths spanned a range from 800 to 1000 nm in 50-nm increments. Typical data collection included an image with no filters, then images were taken with each filter in place, for a total of six images. Background images with each filter were also taken. The analysis of these data, described below, includes side-by-side spatial comparisons and overlays of images of the same CdTe cell using different filters.

Spectral EL measurements were initially attempted on an NREL system set up to take spectral PL data on various types of solar cells. The EL from the CdTe sample, however, was too low to be detected by the system without amplification. The same measurements were taken on a triple-junction control sample, which included GaAs, and EL well above the background noise was detected, indicating that the system was properly set up for spectral EL measurements. The EL signal detected with the Si CCD imaging camera on that same GaAs sample produced very high luminescence (2-3 orders of magnitude greater than the average EL signal produced by a CdTe sample). This indicated that the signal from the CdTe was present but too low for detection on the spectral EL system.

2.3. Analysis of EL Images

Analysis of images provides information about the physical causes and the effects of luminescence. This analysis includes comparing theory and models to experimental data. It also introduces characterization of uniform luminescence signals and non-uniform features related to defects. Categorizing and cataloguing luminescence signatures provides a way to classify small-area PV response. This small-area response includes local defects or inhomogeneities that are inherent in the materials or result from the manufacturing process. The parameterization process is broken up into uniform and non-uniform feature characterization, which includes defining variables and describing the current, voltage, and wavelength response.

A major goal of imaging is to connect the qualitative imaging data with quantitative device parameters to aid in on-line evaluation. This has nominally been done with EL, PL, and DLIT for Si devices [8], [12] and correlations made with Cu(In,Ga)Se_2 (CIGS) [7]. This analysis, however, has not been executed extensively for CdTe, with preliminary reports from CSU [13], [14].

2.3.1. Cell Quality. Data processing began with uniformity analysis. The overall signal uniformity was grouped into three categories: high, medium, and low, as described below. Placement criteria was based on the percentage of the cell area covered by nonuniform features and signal variation. This ranking was subjective but helped sort the data before further analysis.

Cells with luminescence intensity at least twice as large as the background signal at 10 mA/cm^2, little to no gradient in signal, and very few local non-uniformities were placed in the *high* category. These cells were expected to have high efficiency and relatively few

defects. Cells in the *medium* category contained modest signal gradients (noticeable but with intensity changes less than 25%) and local non-uniformities covering 20% or less of the cell. The *low* ranking had cells with severe signal gradients (25% or more), an average intensity less than half above average background count, and local non-uniformities covering more than 20% of the cell. Examples of each are shown in Fig. 2.4.

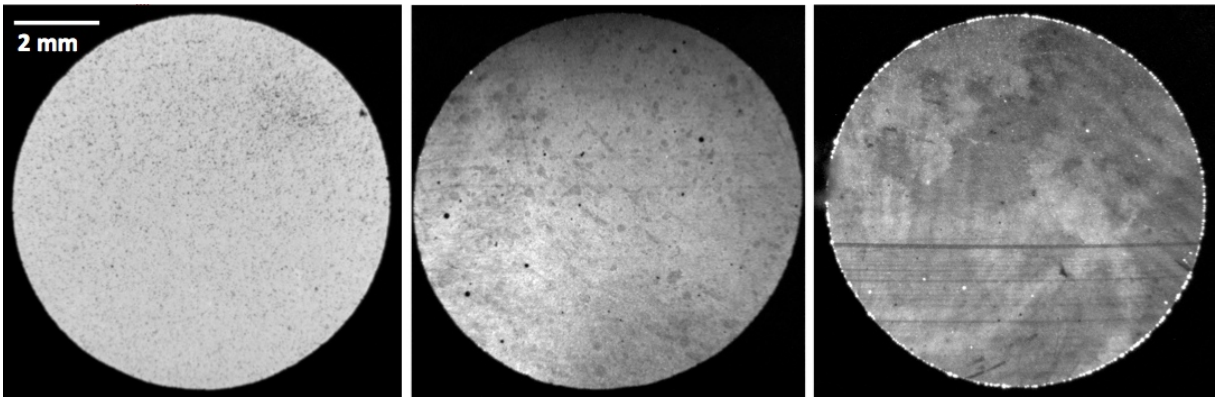

FIGURE 2.4. Examples of CdTe solar cells with EL uniformity described as high, medium, and low uniformity, respectively.

When an intensity gradient is present, indicated by a smooth drop in EL signal over a large portion of the cell, it is generally caused by nonuniform material deposition. In addition, it is common to have significant intensity variation at cell edges, which can be attributed to the delineation process. This is seen in the far-right image in Fig 2.4. There were also subtle patterns that could be seen over the surface of the cells EL, likely due to inhomogeneities in the transparent conductive oxide (TCO) contact layer. (The glass substrates were purchased with the TCO already deposited.) The substrates underwent a cleaning process prior to deposition, and in some cases, the cleaning and general handling of the glass led to residues and track marks that interrupted the TCO layer.

The EL signal depends on cell voltage, as seen in equation 7, so any variations in the voltage will be manifested in the image. This includes variations due to the lateral sheet

resistance of the TCO. This variation in EL due to voltage gradients was seen in models of the EL response and imaging data for CIGS modules, where the voltage drop across the cells due to the lateral sheet resistance effects can be easily seen [8], [10], [15]. An example of this effect at the cell level will be shown in the following section.

The small-area CdTe devices studied here do not have a significant lateral sheet-resistance effect, so focus is directed towards variations in series resistance and TCO resistance. There was also a difference in overall luminescence homogeneity as shown by various patterns that appeared for different samples, as in Fig. 2.4, which were believed to be in the TCO layer (as previously discussed). The variations in the TCO did not have large effects on the overall performance of the cells. The series resistance effects, on the other hand, decreased the voltage but were less noticeable in the images because of the small area that was affected compared to TCO variations. For this analysis, the TCO patterns could, for the most part, be ignored, and the average EL signal related to device V_{OC} as well as other parameters.

Preliminary work showed a clear correlation between EL and certain device parameters for thin-film CdTe devices [13], [14]. The total sample set studied included CdTe devices with a broad range of efficiencies and average EL intensities. Average EL intensity for each cell was plotted as a function of its device V_{OC}, J_{SC}, fill factor, and efficiency on a logarithmic scale. As seen in Fig. 2.5, there are correlations between EL and V_{OC}, fill factor, and efficiency, with the strongest correlation between EL and V_{OC}.

For this particular set of samples, the V_{OC} spans about 100 mV, and the EL increases by almost a factor of two. A similar correlation between EL and V_{OC} with more consistency between sample sets was found at CSU using a different imaging system [14]. In both cases,

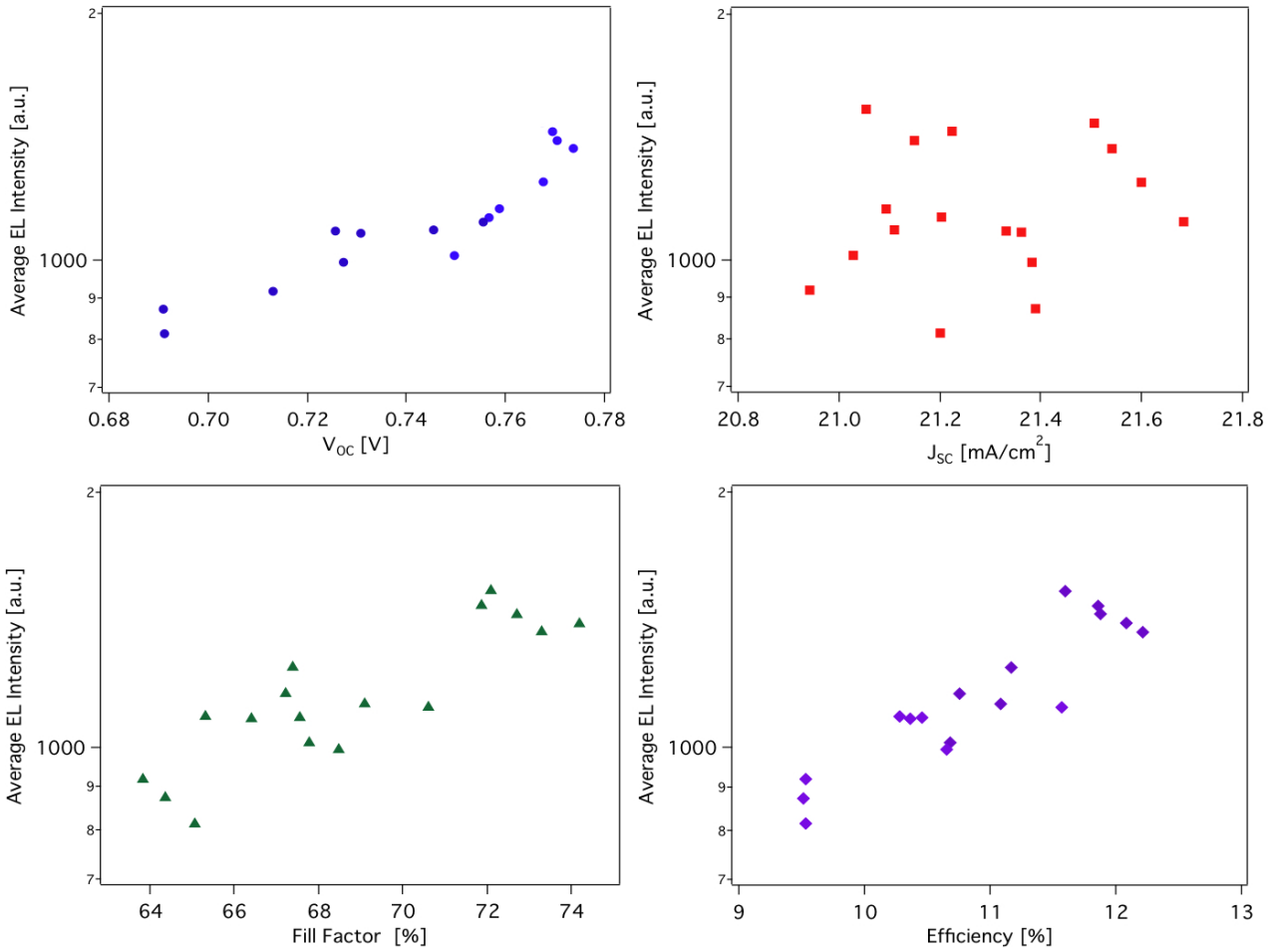

FIGURE 2.5. Plots showing the log of the average EL intensity plotted against device V_{OC}, J_{SC}, fill factor, and efficiency for well-behaved and uniform samples from different substrates. The plots show the strongest correlation between EL and V_{OC}.

there is a reasonable fit to the relation of EL signal to voltage derived by Rau [8]:

$$\phi_{EL} \propto e^{\frac{qV_{OC}}{k_B T}}. \tag{7}$$

This relation held for cells with high and medium overall uniformity. Poor-performing cells and those that were highly non-uniform did not follow this trend. These trends also apply to Johnston's work with CIGS, where a similar but stronger correlation was found between a large set [7].

2.3.2. Current Dependence. The EL signal was sufficient at 10 mA/cm^2 for well-behaved CdTe devices to spatially identify features in EL images, so this was the standard current density used in image comparisons and other analyses. For typical measurements, images were taken at at least three current density values: J = 4, 10, and 20 mA/cm^2. The signal at J = 2 mA/cm^2 was often too low to produce an adequate image. The cells had very unstable voltages and currents at values greater than J = 20 mA/cm^2 so higher current densities were not used to prevent damaging the cells.

The process of looking at the intensity changes with current density through the cell was used to study current response. Expectations included a linear EL response to current density, and in fact, high and medium uniformity produced linear responses. For low uniformity, however, the dependence of the response was often less clear. An example of a medium uniform cell, seen in Fig. 2.6, shows the spatial imaging data for increasing J and the corresponding graph in Fig. 2.7 shows the EL signal plotted with respect to current density for low, medium, and highly uniform devices. The lower row of images in Fig. 2.6, normalized to the current, shows that linearity generally holds, but to a lesser extent in some of the non-uniform regions.

Another good example of EL variation with current can be shown on CIGS lab-scale devices. Because of the effect of the front contact grid on the cells, EL shows a clear voltage gradient across the cell. This gradient becomes more severe at higher current densities, as seen in Fig. 2.8. This is similar to the EL gradient due to changing lateral sheet resistance seen in CdTe and CIGS modules.

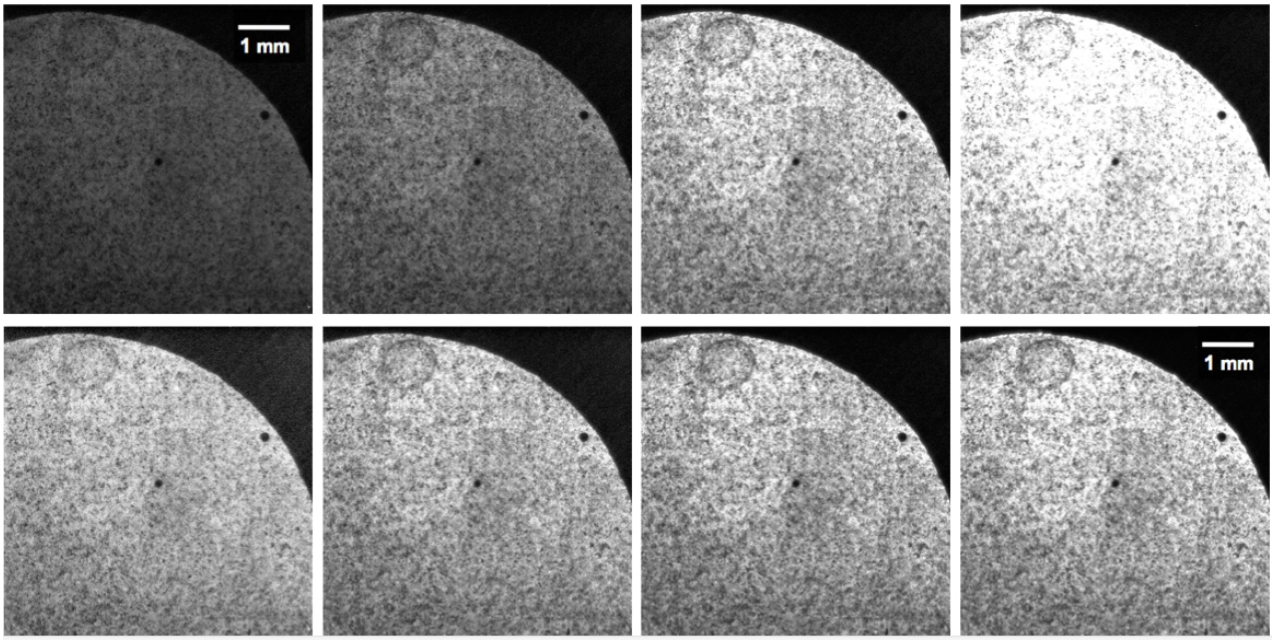

FIGURE 2.6. EL signal at varying current densities for a single CdTe device. Current densities are, from left to right, 2 mA/cm^2, 4 mA/cm^2, 10 mA/cm^2, and 20 mA/cm^2. Top images are shown with the same scale. Bottom images have normalized signal to show similar feature contrast at different currents.

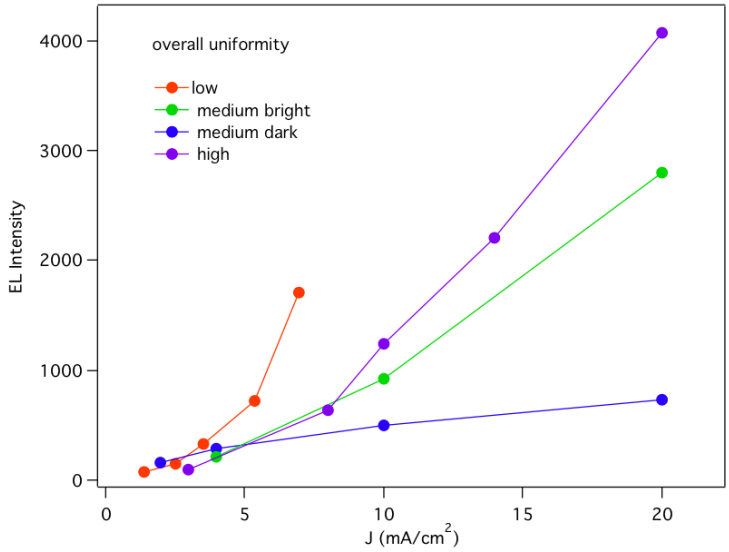

FIGURE 2.7. EL intensity of devices varying in uniformity as a function of current density, J. The response is linear with J for the highly uniform and medium devices.

Another example of current response is the varying EL signal during the first few minutes of biasing the CdTe solar cells. To determine the effects of the applied voltage over time, 10-15 consecutive images with 30 second exposure were acquired. The images showed an overall

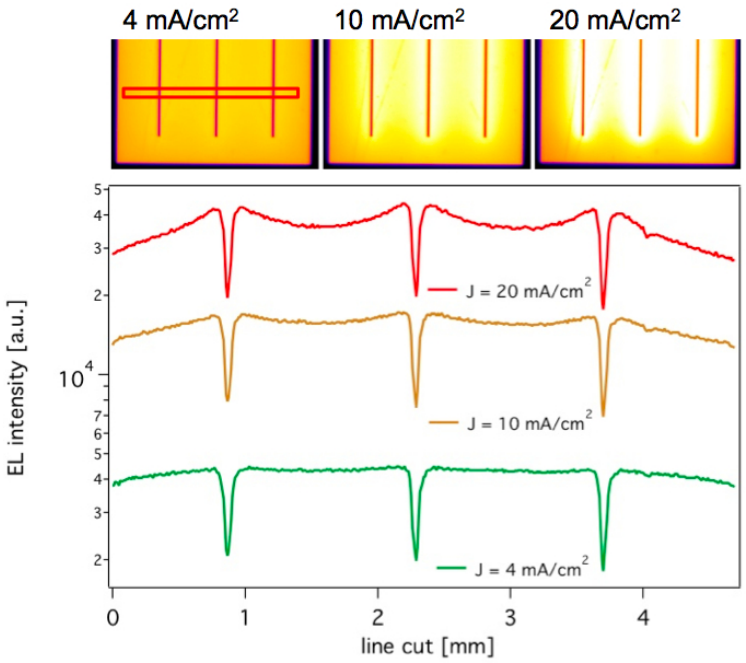

FIGURE 2.8. EL of a CIGS device at different current densities and the corresponding intensity profiles, which shows the increasing voltage gradient due to the front contacts as J is increased.

trend where the overall signal distribution changed significantly during the first minute and very little after that. The first image had a very high intensity relative to the subsequent images. Distribution over the area of the cell was different as well, with the initial image having a larger contrast between areas of high and low intensity. All proceeding images have similar intensity distributions, lower contrasts, and slowly decreasing overall intensity. The difference in the signal distribution and intensities can be seen in Fig. 2.9 with the intensity histograms and EL images.

2.3.3. EMISSION SPECTRUM. Expectations for spectral response were as follows: a large peak centering around the CdTe band gap, 855 nm, would be present. Signals with a lower band gap (and higher wavelength) may be present if there are many defect states between the conduction and valence bands. One would expect little signal to be blocked when the 800 nm filter is used. Less then half of the band-to-band signal would be blocked by the

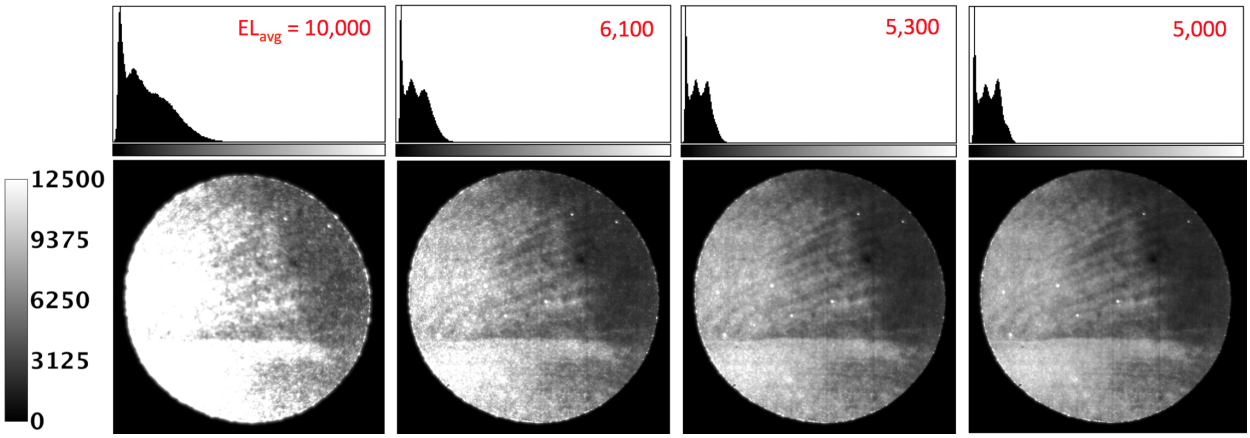

FIGURE 2.9. A series of EL images and corresponding intensity histograms and average EL intensities taken over a span of five minutes for the 9-mm-diameter CdTe solar cells from CSU. The EL signal during the first minute of bias shows overall high intensity and high contrast between areas of low and high signal. The proceeding images have slowly decreasing signal and smaller contrast. Color scales are the same for all images.

850 nm long-pass filter. A larger portion (over 50%) would be blocked at 900 nm, more with the 950 nm filter and more still with the 1000 nm filter.

Initial analysis of the data focused on the change in average EL intensity with filter use. As shown in Fig. 2.10, there is drop in EL signal with the 900 nm long-pass filter and very little signal with the 1000 nm long-pass filter. Fig. 2.11 shows the response of the signal plotted against the values of the minimum wavelengths for each filter that was used for four different samples.

The filter technique focuses on the luminescence signatures rather than spectral details, but the results were close to expected, with the majority of the signal being reduced at higher wavelengths and local EL features seen throughout the image series.

2.4. Specific EL Features

Non-uniformities arise in solar cells that are inherent in the material deposition or result from subsequent device processing. Imaging can be used as a rapid tool to identify where

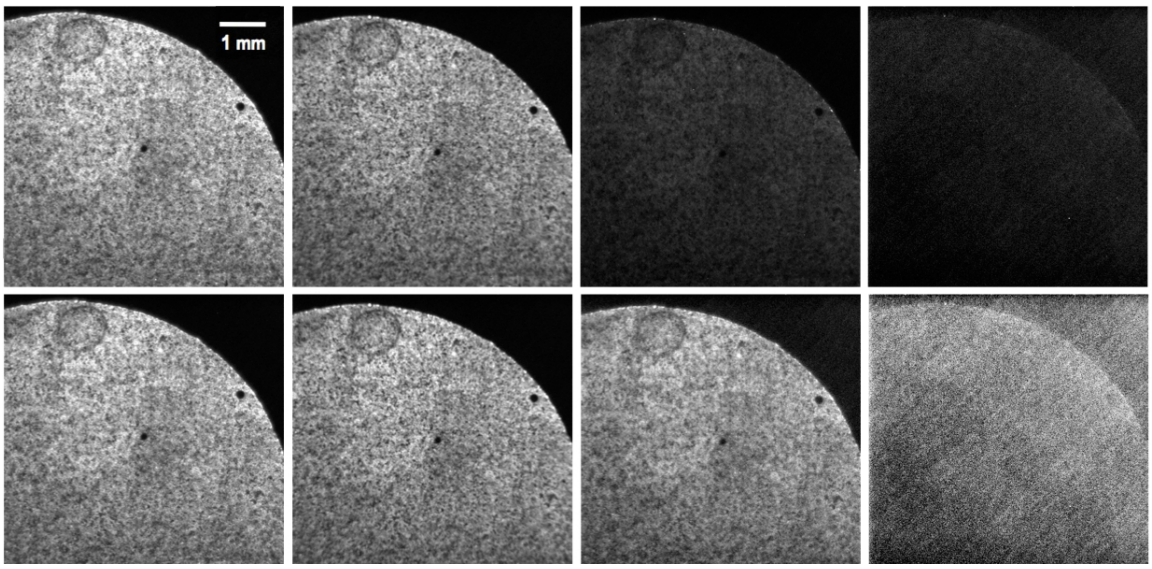

FIGURE 2.10. EL images acquired using long-pass filters. Filters used, from left to right, are: none, LP800, LP900, and LP1000. Top images show the same non-normalized scale to show the large drop in signal at wavelengths higher than 800 nm. Bottom images are normalized to the average EL signal of the device to show similar spectral response of features.

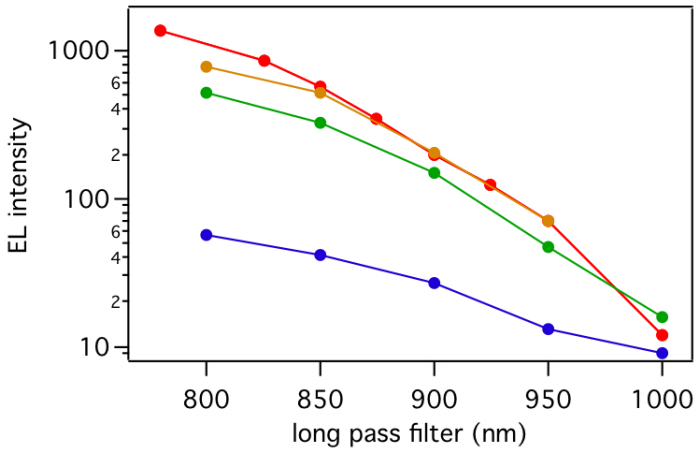

FIGURE 2.11. Average EL intensity plotted against the cut-on value for long-pass filters used to acquire a series of images for several different CdTe devices.

these non-uniformities occur. After EL uniformity is assessed, luminescence signatures resulting from non-uniformities can be identified, described, and further analyzed. Analysis in the previous section included studying spectral responses and voltage and current responses.

This section breaks down the feature types and explores the causes and origins, physical characteristics, and effects on device performance for different luminescence signatures.

2.4.1. Physical Causes. Non-uniformities in EL imaging can be the direct result of variations in carrier recombination. Some of these non-uniformities affect device performance more than others. Identifying the physical causes of these detrimental defects could mean making better devices; feedback can be given to modify processing steps and potentially decrease defects.

Defects can vary in origin and physical characteristics, as described in Chapter 1. Those arising during processing include shunts and weak diodes. These affect current flow, voltage distribution, and will therefore affect the EL signal. Defects which are inherent in the material include traps and high resistances. Traps decrease EL because they result in non-radiative recombination of carriers. Resistances also redirect current flow. There are also other non-uniformities that are not detrimental to device performance but cause changes in EL.

Table 2.1. Possible physical causes of non-uniformities and predicted effects on luminescence.

possible cause	**expected signature**
increased TCO resistance	drop in EL intensity
scratches on glass	dark lines due to obstruction in signal
shunt	dark area which vary in size with changing bias
weak diode	dark spot surrounded by a bright area
fingerprints	dark spots due to signal obstruction
optical/dust	dark because of blocked signal
delamination	no signal

A list of expectations of how these defects and non-uniformities will change the EL signal is given in Table 2.1. In regions where there are dark spots and decreased EL signal, radiative recombination in that region is low. In CIGS, shunts, traps, and increased series resistance

in the window layer are manifested as dark spots [16]. The same is expected to occur for CdTe. There can also be foreign objects or inhomogeneities that optically block the EL signal. This may be more common in CdTe since imaging takes place through the glass in the common supersaturate configuration. Bright spots will occur in regions where there is an increase in radiative recombination. This may be an effect of increased current or decreased resistance. Edge effects can also result from poor device formation with the blasting process, as explained in Chapter 1.

Effects of shunts and weak diodes have also been studied in Si and CIGS imaging. As seen in thin-film CIGS, the impact of shunts and weak diodes extend beyond the actual defect size [10]. The highly conductive path of a shunt draws down the voltage of the surrounding area, causing current to be diverted towards the defect. This is manifested in EL images as decreased signal, as a direct result of the drop in voltage. Furthermore, as the bias increases, the area affected by the shunt increases. Weak diodes also result in lower voltages and direct the flow of carriers towards the defect at much lower biases than normal. These effects are similar in CdTe devices.

Previous models explore the voltage and current distributions, including the bias dependences, of shunts and weak diodes in both thin-film technologies [10]-[17]. This work predicts the effects on luminescence based on the models and known device physics. Possible causes of luminescence inhomogeneities and subsequent EL signatures, as seen in Table 2.1, are described in the following section.

2.4.2. Signatures. Identifying and cataloguing specific features were part of the EL analysis. Luminescence signatures varied in shape, severity, and area of the cell that was affected. Overall, there were two general types: dark areas of decreased luminescence and

bright regions where luminescence was higher. Some features were specific to CdTe and some overlapped with other technologies.

For cases of decreased luminescence, there were large gradients across the entire cell where one side had less signal. These were the result of nonuniform material deposition during manufacturing, as mentioned earlier. The decreased layer thicknesses, especially in the CdS layers, decreased the voltage in those areas. There were also dark circular patterns, which could be classified as "spotty", and more streak-like dark regions that covered portions of the cells. Some of the patterns were faint and some quite distinct. The circular features, which occurred the most frequently in the devices, were a result of the TCO cleaning process. The streaky patterns were the result of poor handling of the TCO/glass during TCO deposition, packaging and shipping, and handling before deposition.

There were also local dark spots in the interior that varied in size and edge contrast. Typical sizes of these dark spots were 100-250 μm. Causes of these particular signatures ranged from foreign objects (such as dust) on the glass that acted as optical blocks, to disruptions in the material layers, including shunt-like defects and foreign matter disrupting the material deposition. There were also dark scratches that were infrequent but very distinct. These were likely located on the TCO/glass.

Local bright features that were located in the cell interior tended to be less frequent and smaller than the dark signatures. The sizes of the local interior spots were 50-150 μm. Their causes were unknown but it was predicted that weak-diode-like defects would consist of a dark spot surrounded by a bright region, as seen in the pronounced features in Fig. 2.12. Many of the bright spots were very small, so it was likely that if the feature resembled a weak diode it would be difficult to tell because the dark spot was not distinguishable (unlike the

examples shown in the figure). Bright edge effects seen at higher current densities ranged from 50-100 μm and resembled small, individual spots on the circumference of the cells or groups of connected spots that outlined the edge. They were the result of poor edge processing when the individual cells were made, although further details were unknown. An example of a CdTe EL image with dark and bright spots as well as the bright edge effects are seen in Fig. 2.13.

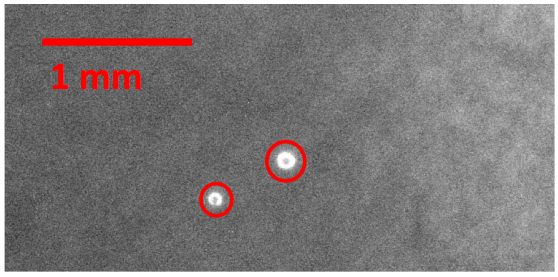

FIGURE 2.12. Weak-diode-like luminescence signatures seen in an EL image of a CdTe cell. These features, seen highlighted in red, are larger than typical so as to distinguish the dark spot surrounded by the bright ring.

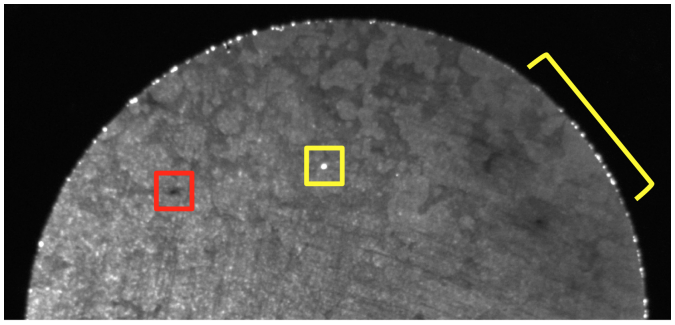

FIGURE 2.13. EL image of a 9-mm-diameter CdTe cell showing several signatures, including bright and dark spots in the cell's interior (boxed in yellow and red, respectively) as well as bright edge effects (highlighted in yellow). This cell also has the cleaning residue on the TCO as seen by the pattern across the top portion.

Many of the variations that were seen in EL images resulted from inhomogeneities in the TCO layer, as previously described. There were more interesting features, however, that could arise as EL signatures which occur in the window or absorber layers or throughout the entire cell. These included shunts as well as areas that behaved like weak diodes. As

mentioned before, previous studies have been done on thin-film solar cells, particularly CIGS, that predict how these non-uniformities affect EL signal [10], [18]. Experimental results on thin-film modules have also been reported [18]. Shunt detection in this study began with identifying dark spots in EL images. Knowing that shunts affect different areas at different biases, two images of the same cell at different current densities were divided by one another to see if the dark regions changed sizes with biases. This led to the finding that most of the local dark spots seen in EL images of small-area CdTe devices were not shunts. More in-depth analysis using dark lock-in thermography paired with EL will be discussed in Chapter 5.

2.4.3. Variation with Current and Wavelength. Voltage and current responses were evaluated when studying the different types of luminescence signatures discussed above. Rough spectral information was also acquired on the signatures with filter use. Changes in overall intensity of the signature and the surrounding areas were measured. Line cuts which yielded intensity profiles were also a good measure of changes in intensity in the regions surrounding features of interest, for both spectral and current response measurements.

Intensity profiles helped to distinguish features that grew in size with bias, stayed the same size, or affected surrounding regions. Profiles were constructed in ImageJ. Line cuts were made by highlighting the region of interest with a straight line, with the size of the line measured in pixels. Pixels were then converted to microns. A profile plot was then made which showed the EL intensity as a function of distance in microns. Curves for each cell were plotted on the same graph and compared.

Plots provided current and wavelength dependence for luminescence intensity for the signatures. For most dark features, current dependence showed that the areas immediately surrounding the spots were not affected by the feature and EL responded linearly with

current density, with the spot size remaining constant. The same was true for bright spots, with surrounding areas unaffected and spots not changing size or only slightly increasing with increased current. An example of an intensity profile across a dark and bright spot and the corresponding current and wavelength responses are shown in Fig. 2.14.

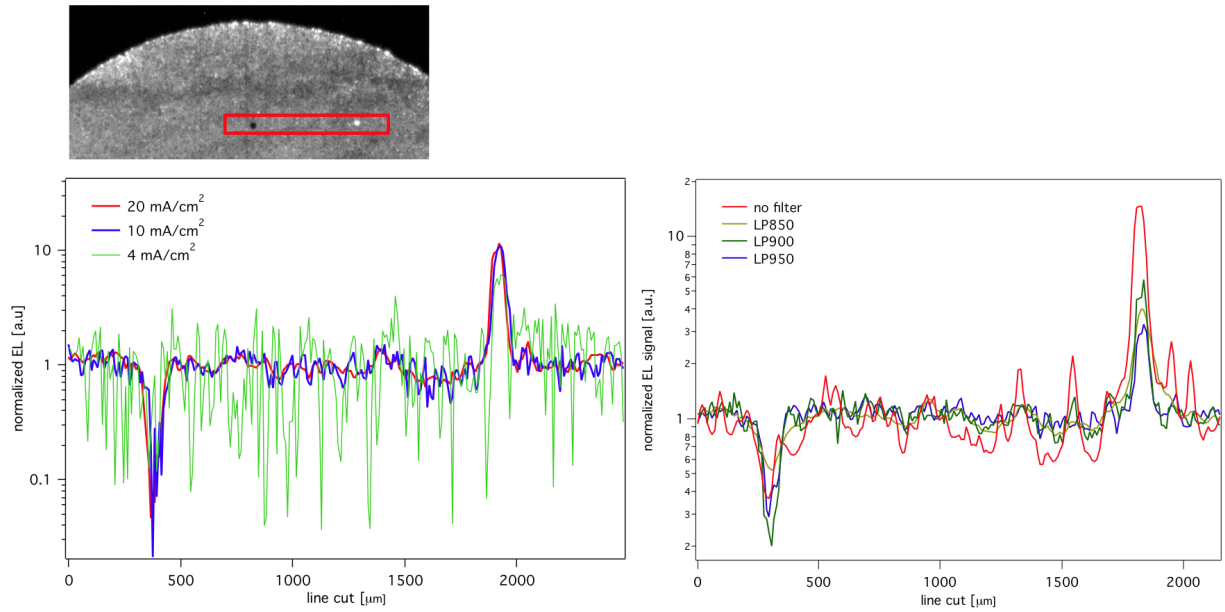

FIGURE 2.14. An EL image and corresponding EL profiles of interior dark and bright signatures in a CdTe cell. The box in the image highlights the location of the line cut, which was approximately 2 mm wide. The first plot shows current response, while the second plot shows the response as a function of long-pass filter cut-on wavelength. The signals were normalized to uniform luminescence.

The plots shown in Fig. 2.14 were normalized to a uniform region away from the feature so that the signature response could be directly compared to the regions of normal luminescence for that particular device. The circular dark feature was approximately 90 μm in diameter. Its size stayed constant with changing bias. The intensity profiles acquired with filters showed that the size of the spot was unchanged and the region directly surrounding the spot had a similar response to uniform areas. The bright spot was 75 μm in diameter and had a constant diameter as current density through the cell changed. Spectral response shows that the luminescence surrounding the spot was very similar to the normal luminescence.

Edge effects were also studied. These bright spots often appeared at 10 mA/cm^2, but sometimes began to show as early as 4 mA/cm^2 if they were more severe. Current response of the edge effects was more sensitive to increasing bias than more uniform luminescence. The spectral response, however, was similar to normal luminescence, as seen in Fig. 2.15. The tail of the signal response seen at higher cut-on wavelengths is the same as the uniform signal in the cell's interior. The ratio of the edge intensity to interior intensity is approximately 2 for $J = 20$ mA/cm^2 and between 1.5 and 2 for $J = 10$ mA/cm^2.

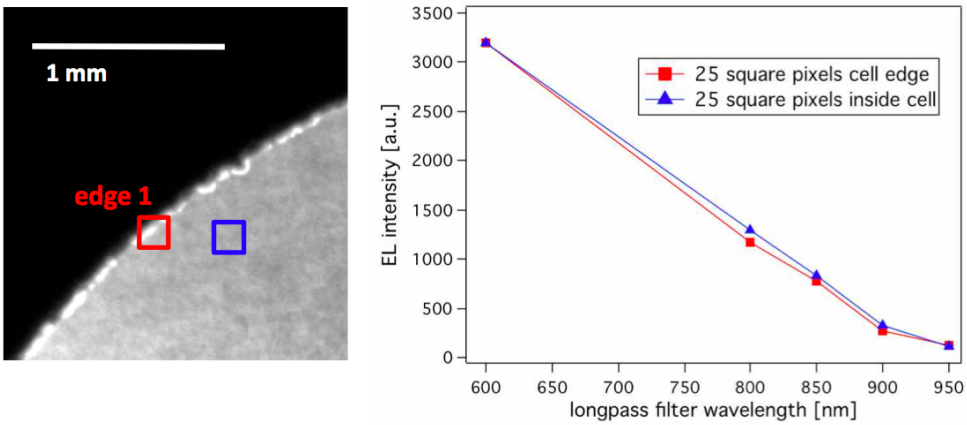

FIGURE 2.15. An EL image of a CdTe cell edge that exhibits bright edge effects. The two boxed regions were selected for a rough spectral study. The resulting EL intensity as a function of long-pass filter wavelength is plotted on the right.

Further exploration of these EL signatures is presented in later chapters, including combining other techniques with EL to offer a more detailed explanation of their physical effects. Further correlations will also be found in hopes of using imaging to predict device efficiency.

2.5. CONCLUSIONS

EL imaging as a characterization method is straightforward and fast, and even first-order analysis makes this technique valuable. The images provide spatial information about carriers moving through a cell, whereas the analysis provides a way to begin quantifying the data.

EL on small-area CdTe devices made at Colorado State offers a solid platform for characterization of images from thin-film solar cells. Calibrations of the CdTe images taken with NREL's Si CCD camera were done to compare with data taken with other cameras. CdTe images were classified based on overall uniformity of the luminescence signal. EL intensity was also compared to device performance to determine correlations with cell quality. In practice, however, many of the non-uniform features seen in EL, such as the slight variations in signal the TCO, do not greatly affect the device performance. Distinct luminescence signatures were also identified, which offered additional information on the causes and effects of inhomogeneities, as well as current and spectral responses.

There were 200 CdTe samples measured using EL, with over 1,400 EL images acquired. Results presented here, including parameterizing and the correlations, are largely empirical. The next step would be to move to a more quantitative analysis of the imaging data. Even without the quantitative analysis, however, EL is seen to be particularly revealing for CdTe cells. In particular, it allows material inhomogeneities and poor devices to be quickly identified. When coupled with lock-in thermography and other characterization techniques, as explored in later chapters, EL becomes even more useful.

CHAPTER 3

Photoluminescence Imaging

Photoluminescence, or PL, does not require a semiconductor junction or contacts, and therefore has the potential to be useful as an in-line evaluation tool during cell or module fabrication, after the deposition of the window layer or the absorber material. The camera detects radiative recombination of excess carriers generated by an illumination source. The resulting image provides spatial information about carrier recombination. In this way, PL shows changes in the electro-optical properties of key layers of a solar cell, including defects due to shunting and variations due to local series resistances [5]. Changes in carrier lifetime are also reflected in PL, as shown with PL measurements of CIGS and Si [7], [19].

Since PL does not require a full device, poorly performing cells can be identified before construction is completed, and processing can be aborted early, saving energy, materials, and money. There was an initial limitation, however, in this PL study of CdTe. While this technique was developed at the National Renewable Energy Laboratory (NREL) to image both silicon and Cu(In,Ga)Se_2 solar cells, the system was not well equipped to measure CdTe devices (because of the lack of filters and illumination sources suitable for CdTe). One goal of this work therefore was to develop PL imaging for CdTe at NREL, focusing on acquiring the best excitation sources and filters.

3.1. Experimental Setup

Photoluminescence imaging uses an external illumination source to excite excess carriers in a photovoltaic device, detecting the resulting photons given off as luminescence when the carriers recombine. The PL setup at NREL uses the same Si CCD camera as the

electroluminescence (EL) imaging system to produce the images. The illumination source depends on the band gap energy of the solar cell being measured; the external light must have enough energy to excite electrons in the absorber material from the valence band to the conduction band.

Measurements on CdTe began with a set of four 630-nm 5-Watt Digi-Key light-emitting diodes (LEDs) for the excitation source. Since CdTe has a band gap energy of 1.47 eV, which corresponds to a wavelength of approximately 843 nm, the 630-nm photons contain sufficient energy to excite carriers across the CdTe band gap. Illumination intensity from the LEDs was adjusted based on the amount of desired excitation. Illumination power corresponding to one sun (100 mW/cm^2) was taken as the standard. One sun corresponds to the intensity of photons at that particular wavelength at AM1.5, the air mass spectrum of the sun incident on the surface of the Earth. Adjusting the power of the illumination source allows for imaging at different levels of carrier injection, as discussed below.

Filters, along with the illumination sources, were an integral part of the system. They were used to block reflected LED light from the stage area, and could easily be interchanged as needed. The selection of the filters depended upon the wavelength of the excitation sources, which was to be blocked, and the wavelength of the PL emission, which was to be transmitted through the filters to the detector. The setup usually consisted of one long-pass filter with a suitable cut-on wavelength, but more than one filter (such as a combination of long-pass and short-pass filters) could be used.

The filters were attached to the lens of the camera, which was mounted on a translational vertical post looking down on the stage. The CdTe solar cells were placed on the stage on a non-reflective surface. The illumination sources, mounted to adjustable arms, were on the

outside of the stage area and directed towards the sample. The complete setup, including the camera, light sources, and sample, is shown in Fig. 3.1.

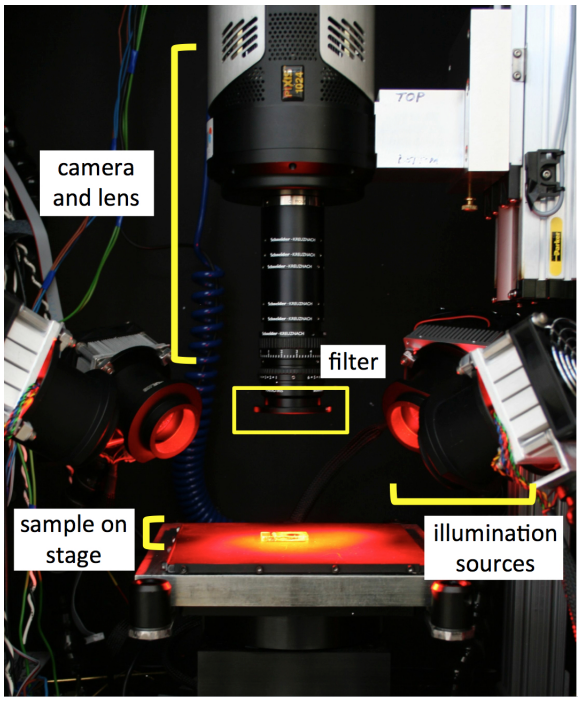

FIGURE 3.1. NREL's PL setup, including the CCD camera and 630 nm LEDs. The LEDs emit a red light, which appears artificially yellow on the sample where the light is most concentrated because of the image contrast.

An in-depth presentation of the use and outcome of different filters is presented in this chapter. Various illumination sources were also acquired and tested in later measurements, the results of which are also presented.

3.2. EXPECTATIONS

PL imaging is used to provide spatial information for CdTe, much like EL. It is expected that similar features will overlap between the two techniques as discussed in chapter 5. One difference between PL and EL, however, is that PL has been related to lifetime in other PV technologies such as Si and CIGS [7], [19], whereas EL was found to be linearly proportional to minority-carrier diffusion length [7]. While lifetime (τ) and diffusion length (L) are related

as $L \propto \sqrt{\tau}$, the dependence of PL to lifetime and EL to diffusion length were the strongest correlations found. EL is also affected by series resistance, whereas PL is not. So some differences between EL and PL images are to be expected. PL, unlike EL, is a contactless method. Therefore it does not require a complete device with contacts.

The majority of the emitted photons are expected to have energies similar to the CdTe band gap, 1.47 eV. Electron-hole recombination occurring primarily across the conduction and valence bands will emit photons around 1.47 eV. Donor and acceptor states within the band gap may contribute to reduced emission energies. There may also be some emission at lower energies because of CdSTe that forms through sulfur diffusion in the absorber layer during processing. Other alloys and the presence of defect states may also influence emission.

With PL related to minority-carrier lifetime, one would expect to see variations in PL for CdTe due to differences in lifetimes values with varying deposition parameters. Higher-quality material and longer lifetimes should have a higher proportion of radiative recombination compared to non-radiative, which would increase the PL signal. Radiative recombination, and therefore PL signal, is dependent upon doping. Within a sample, it is assumed that the doping is constant so there is little or no variation in PL signal due to this effect. Optical properties such as reflectance also affect PL signal. The various effects related to CdTe are discussed in the following section.

While external illumination is used to excite carriers, the light penetrates only a shallow distance ($\sim$ 100 nm) into the CdS/CdTe layers. The majority of the photons pass through the glass, TCO, and CdS layers without being absorbed. Absorption begins at the CdS/CdTe junction, within the depletion region, and continues into the first few tenths of a micron of the CdTe. Changes in the electric field in the junction region will affect where carriers recombine,

so one must consider the size of the space-charge region, field strength, and number of incident photons, and the density of carriers generated. This was explored using PL lifetime data and simulations at NREL, where relationships between the PV parameters, measured lifetimes in thin-film solar cells, and PL emissions have been previously reported [20]. Because of the sensitivity to small changes at the junction, the PL signal is affected in ways that cannot be fully predicted or quantified.

3.3. Data Acquisition

The PL setup at NREL was optimized for measurements on Si and CIGS devices when it was initially built. When the original PL imaging system was applied to CdTe samples, it was partially successful, but detailed development of the system for CdTe and in-depth analysis of CdTe data did not begin until this study.

Initial equipment for CdTe included the 630-nm LED illumination sources. Different camera filters that were used to block reflected light and allow the PL signal to be transmitted to the detector included long- and short-pass filters, with a set of long-pass Schott glass filters that were typically used for Si and CIGS imaging. The configuration with the 630 nm LEDs and Schott glass filters allowed for the successful acquisition of PL images on CSU's CdTe devices. There was an initial question, however, as to how much of the signal was actual luminescence and how much reflected light from the sample and stage area was still being transmitted through the filter and into the detector. The successful separation of PL signal from reflected light was achieved by varying illumination intensity, exposure time, and filter use to study signal response.

Examples of PL images for different technologies are presented in Fig. 3.2; the same Si, CIGS, and CdTe solar cells that illustrated EL in the previous chapter are shown. The

images were acquired using the PIXIS Si CCD camera, and the data are stored and analyzed using Image J software.

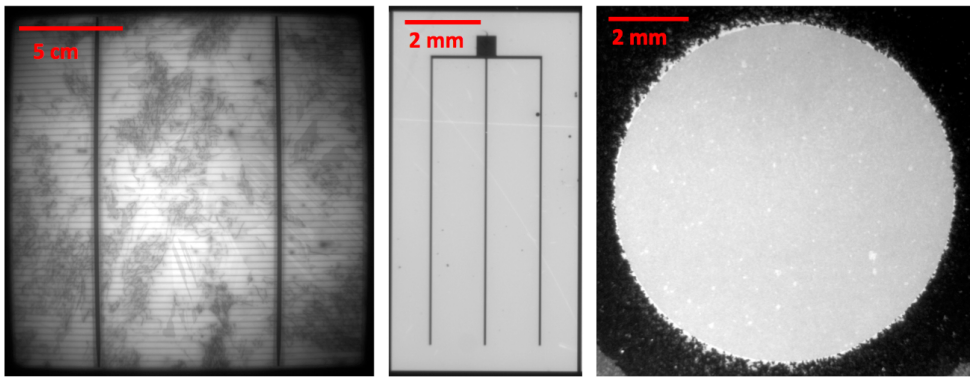

FIGURE 3.2. PL images of the same Si (left), CIGS (middle), and CdTe (right) solar cells shown in Fig. 2.3. Note that the Si cell is much larger.

The Si sample in Fig. 3.2 shows grain boundaries, which do not appear in CIGS and CdTe because of their much smaller grain size (0.5-2 μm) and the limited camera resolution. The Si image also shows inhomogeneous illumination because of the large sample size; it is difficult to get an illumination area to sufficiently and uniformly cover the 20 cm $\times$ 20 cm Si sample. The CIGS sample shown here is quite uniform except for the contact fingers. However, there are three small dark spots that can be seen near the right grid finger, as well as a bright scratch across the width of the cell. These features can also be seen in the EL image. The CdTe sample, on the other hand, does not show the detail in PL that was present in EL. The PL image contains small bright regions scattered across the entire cell that did not appear in EL, but can be seen in the optical image taken in room light. The differences seen in EL and PL of CdTe, along with comparisons between imaging and other characterization techniques, are discussed later.

3.3.1. EXCITATION POWER AND EXPOSURE TIME. Variations in illumination intensity were used to quantify the PL signal. The standard PL measurements used an incident

power similar to one sun, but the LED intensity could be adjusted to provide higher or lower illumination power. For varying illumination intensities, it was expected that the PL signal increases approximately linearly with incident power up until the "high injection" threshold, where the illumination becomes high enough to change the number of holes in the CdTe. The physical affects of this are a changing electric field and the number of carriers that can be generated, and therefore a change in PL.

The normal operation of a solar cell is at low injection, when the number of generated carriers is low compared to the majority carriers. The minority carrier recombination rate is also linear. High injection conditions, which are unfavorable, cause non-linear behavior. High injection occurs when the photogenerated density, $G\tau/\alpha$, is greater than the hole density:

$$\frac{G\tau}{\alpha} > p, \tag{8}$$

where G is the generation rate, τ is lifetime, α is the absorption coefficient. PL measurements should be done at low injection. Therefore the photogenerated carrier density needs to remain smaller than p for CdTe.

Minority carrier lifetime for CdTe is on the low end, usually on the order of a nanosecond. Typical values for the other parameters in CdTe, G (at 30 mA/cm^2) $\simeq 2 \times 10^{17}$ cm^{-2}s^{-1} and $\alpha \simeq 2 \times 10^{-5}$ cm, lead to high injection for a hole density on the order of 10^{13} cm^{-3} or less. This implies that the change from low injection to high injection is not very strong. Often times, the lifetime τ is the dominant factor because carriers recombine almost as fast as they are generated. So a good, steady population never has the opportunity to build up if the lifetime is too low.

The relation between PL intensity and illumination intensity is shown in Fig. 3.3. There are ten CdTe cells shown on this plot from four configurations of cell layers, each with different processing conditions. The corresponding PL images for one of the samples in the plot are shown in Fig. 3.4. An optical image taken at room light is also shown to compare features seen in PL and non-PL conditions.

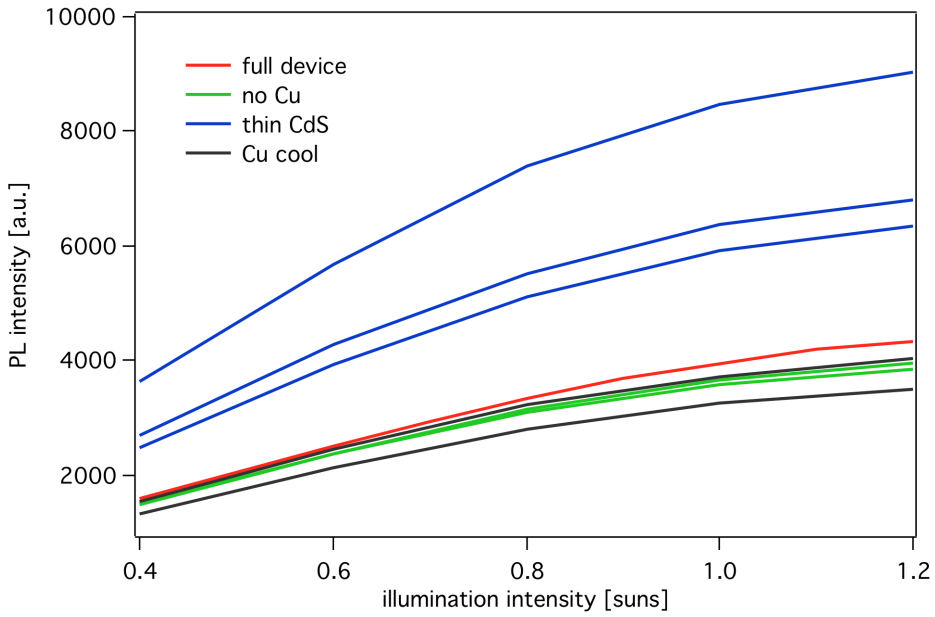

FIGURE 3.3. PL intensity as a function of illumination intensity for various CdTe solar cells.

Varying the injection levels may provide additional information as to how carriers are generated and recombine. A trend in PL response is clearly present. There is a steady increase in PL signal up until one sun, but above that, the rate of increase is reduced, suggesting the approach to high injection. The low to high cross-over occurs at intensities somewhat above one sun, as seen in the change in PL response in Fig. 3.3. Intensities exceeding 1.2 suns were not achievable because of the limited output of the LEDs, and were not desired because of the approach to high injection. The spatial variations seen in Fig. 3.4 are not numerous but are common in CSU's CdTe samples. The bright spots that can be

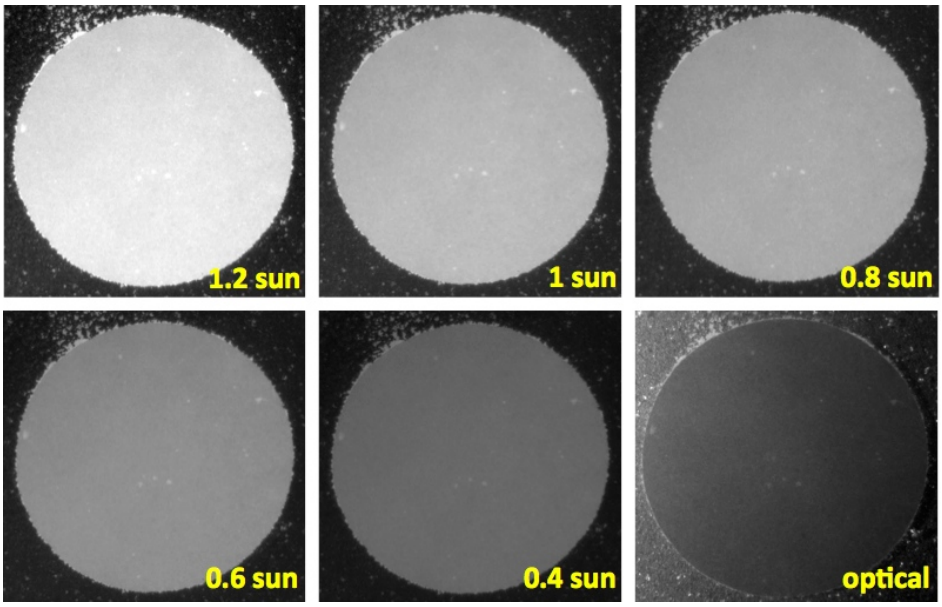

FIGURE 3.4. PL images of a 9-mm-diameter CdTe cell at varying illumination intensities, showing the overall change in signal and the small nonuniformities that can be seen at all levels of illumination. An optical image taken with room light is also shown at the lower right to contrast the luminescence features.

seen in the cell, both in the PL images and the optical image, are reflections that are likely due to inhomogeneity in the glass/TCO. The bright edge effects seen in PL (and the optical image) are reflections from material that was not fully removed from the glass during the cell-delineation process.

Additionally, there are optical effects which will change PL. It is unknown exactly how the reflected light will change the detected signal, but if there is more reflected light falling on the stage area or more of it is transmitted by the filters on the camera lens and reaches the detector, it will skew the data. The background in the PL images of CdTe samples using the RG1000 (1000 nm long pass) filters is between 1000 and 2000 counts. If there are twice as many incident photons on the sample and stage area, there should be twice as much reflected signal being detected. Also, if a different filter is used which transmits more of the

reflected light, it will be difficult to distinguish actual PL signal with the signal coming from the illumination source.

Exposure time was also varied to study signal response. As initially assumed, this behavior was linear for most of the CdTe samples studied. An example of a well-behaved sample can be seen in Fig. 3.5. As far as expectations go, if the incident power remains constant, the overall signal should not be affected by the reflected light, which remains at the same power. Cells have a direct linear response for exposure time (once background signal is subtracted out) unless they are so poor that very little signal is seen.

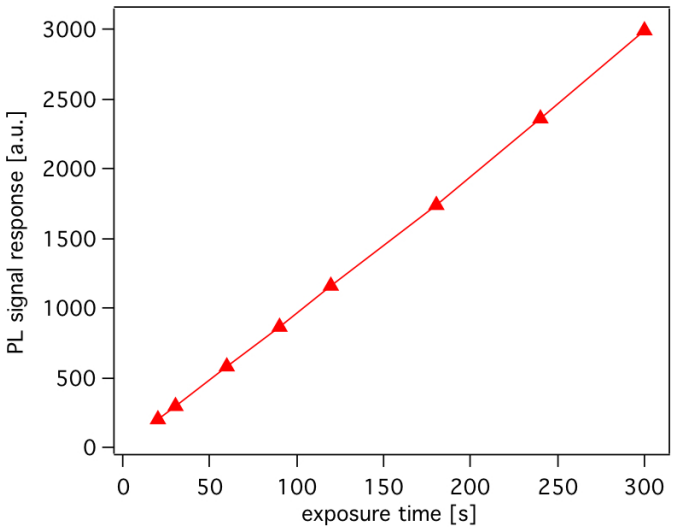

FIGURE 3.5. PL intensity as a linear function of exposure time for a standard (well-behaved, uniform) CdTe cell, with the background signal subtracted out.

3.3.2. FILTER STUDIES. Filter studies were done by using different filters in various configurations to see which produced the clearest image. The goal was for the filters to block as much of the reflected illumination and transmit the largest PL signal as possible. Because of the larger band gap, the wavelength cutoff for the filters with CdTe is not the same as that used to image Si and CIGS.

The filters tested included a set of short- and long-pass filters from Edmund Optics that had a range of cut-on and cut-off wavelengths. There were also a set of Schott glass filters which have different cut-on wavelengths and a few solid-state filters, including InP and GaAs wafers which were typically used for Si and CIGS. Along with the appropriate transmission spectra, the filters had to have an adequately high optical density to sufficiently block reflected light. For this reason, more than one of the same type of filters were in some cases stacked together.

A primary issue related to the long- and short-pass filters was their angle sensitivity. Illumination striking the sample had a significant angle of incidence (as large as 45 ° from the vertical). This meant that a portion of the reflected light would be transmitted. The Schott glass filters were less sensitive to the angle of incidence and were therefore better at blocking reflected light.

The Schott glass filters used included three stacked RG715 filters (where RG means that a red glass, which transmits IR light, was used as a base of the filters, and 715 indicates the cut-on wavelength in nm). One RG715 had internal transmittance of 98% between 800 and 850 nm and less than 10% at 630 nm, which should allow transmittance of most of the PL signal from CdTe while blocking more than 90% of reflected light from the illumination source. Other Schott glass filters also used included RG850 and RG1000. The results of the filter study are reported below.

Visually, some filters proved more useful than others by providing more contrast between cell and background. Most of the filters tended to show the same spatial detail, while it was apparent that the Edmund Optics short and long-pass filters transmitted much more reflected light. This was shown through the inhomogeneity of the signal seen in the images,

including shadows across the cells that were caused by internal reflection of the light through the 3-mm thick glass substrate. The RG715 filters provided similar spatial information as the RG1000 filters but showed more reflected light. The InP and GaAs filters also show similar spatial variation but much higher signal and a higher background count, indicating that much of the detected signal is reflected light. Figs. 3.6 and 3.7 show PL images of a CdTe cell taken with Schott glass, InP, and GaAs filters and the filters' corresponding transmission curves.

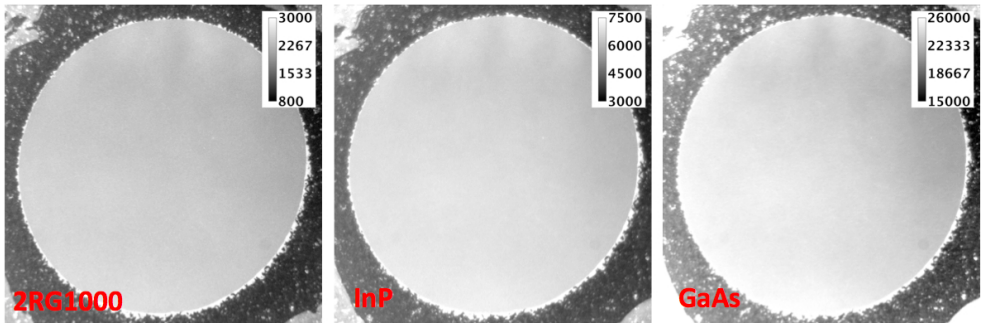

FIGURE 3.6. PL images of a 9-mm-diameter CdTe device taken with three different types of filters (*from left to right*): 2RG1000, InP, and GaAs. Scales are shown for each image.

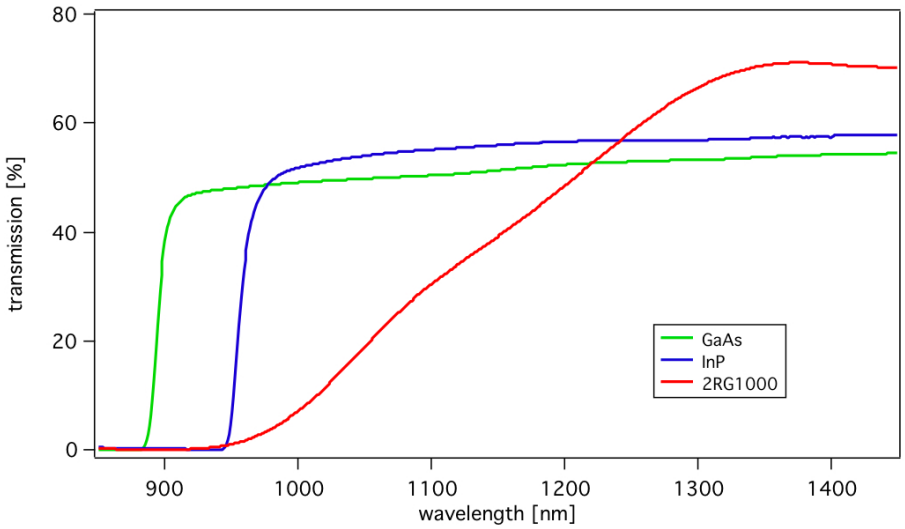

FIGURE 3.7. Transmission curves for the three filters used in Fig. 3.6.

After collecting data with the filters that were on hand, a request was made for a special custom AlGaAs solid state filter; a group from NREL created a 1.59-eV filter to block the

630-nm light source but allow for more transmittance of PL signal. AlGaAs has a direct band gap that can be tuned with a minimum energy of 1.4 eV (GaAs) and a maximum energy of 1.9 eV (AlAs). Bier's law was used to determine the thickness needed to block over 90% of reflected light; two 12-μm films would provide an optical density over OD8. But there were serious problems making the films. The adhesive used on the substrate to grow the films caused bubbling. The optical and spectral properties of the adhesive were also unknown. When films thicker than 15-μm were grown, they showed signs of spalling (flaking), so thickness was limited. Once the three targeted 12-μm films were finished and tested, they contained pinholes throughout the material. This caused sufficient transmission of reflected light into the detector in circular patterns to disrupt the images. As a result, the photoluminescence signal was low and had little contrast against the reflected light, which was transmitted through the pinholes. Even after covering the visible pinholes with black caulk, too much of the reflected light was still transmitted.

3.3.3. Illumination Sources. Different external illumination sources suitable for measurements on CdTe were tested throughout this study. A set of 810-nm laser diodes, used for imaging Si and CIGS, provided strong, single wavelength excitation. However, since CdTe has a higher band gap, the 810-nm laser diodes were insufficient to excite carriers and were not used for CdTe. At the time that the system was built, shorter-wavelength laser diode sources were not available for CdTe. As a result, a set of 630-nm LEDs were purchased for CdTe measurements. But the combination of these light sources and the filters available proved less than ideal for allowing PL emission to be transmitted and reflection from the LEDs to be blocked. As discussed above, PL images showed some PL signal from the cell and considerable background reflection of the LED light reflected from the sample and stage

area. As a result, several other excitation sources, including other LEDs, laser diodes, and HeNe and YAG lasers, were used for PL measurements on CdTe.

Two HeNe lasers, one red and one green, were tested. Each had beam diameters of approximately 2 mm and power below 5 mW. Because of the weak laser power, the luminescence signal was also weak and because the spot size incident on the samples were very small, and background reflection was still very high. The next illumination sources tested were Prizmatix LEDs (with a peak wavelength of 635 nm) and four small DigiKey laser diodes (at 650 nm). The LEDs had the most power, with illumination exceeding one sun. The laser diodes were a little weaker, with a signal between one half and one sun. Even with the use of the Schott glass filters as well as an InP filter, the amount of reflected light remained high for both.

Continuing with the optimization of the PL setup for imaging CdTe solar cells, a 532-nm pulsed YAG laser was tested as an illumination source. Three RG715 filters were used to block reflected laser light. Since the original spot size directed onto the sample was small (1 mm^2 for a 0.7 cm^2 sample), diffusers and other optics were tested to spread the beam. Despite success in expanding the illumination area, there were diffraction patterns from the lenses. Despite the pattern, distinct nonuniform features could be seen, along with a slight variation in signal. A convex lens and beam splitter were then added, which decreased the severity of the diffusion pattern but still had a nonuniform illumination area. The PL images produced with the LEDs, laser diodes, and 532-nm YAG are seen in Fig. 3.8.

Of the sources investigated, the 640-nm Prizmatix LEDs provided images that were spatially most like those acquired with the 630-nm LEDs. The 532-nm laser, however, produced the highest signal, with the CdTe samples having a signal that was four times

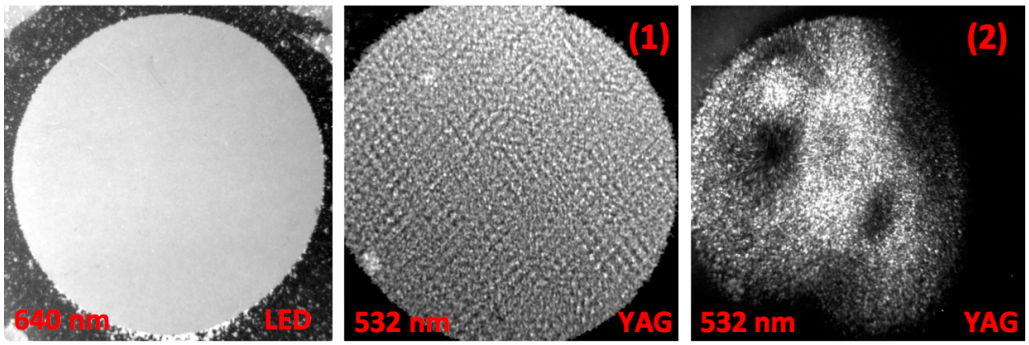

FIGURE 3.8. PL images of a 9-mm-diameter CdTe cell showing two illumination sources that were tested throughout this study. The image on the left was taken with the 640-nm Prizmatix LED, which had a 650 nm short-pass filter on it to block higher wavelength light. The images in the middle and right were taken with the 532-nm YAG laser. The middle image, (1), used a diffuser to spread the beam. The entire cell was excited but there was a pattern that unfavorably disrupted the signal. The image on the right, (2), used an additional convex lens and beam spitter in hopes of spreading the beam more uniformly. This provided even more nonuniform excitation than with the diffuser.

greater than the background. This is an improvement over the previous images produced with the 630-nm LEDs, which showed a very weak signal. If we were to acquire a green laser (on the order of 530 nm) with a uniform spot size on the order of the CdTe cell area, this would improve the PL system for CdTe imaging.

3.4. Analysis

3.4.1. PL Signatures. PL signatures are spatially much like those seen in EL, although the amount of detail seen in EL images of CdTe is not generally seen in PL. PL features do not appear as frequently as in EL, but variations in signal are distinguishable. This may be due to the excitation source penetrating only a small portion of the bulk, with the majority of the carrier separation and recombination occurring in the first few microns of the CdS/CdTe layer. In EL, the bias is placed across the entire device and so separation and recombination takes place over most of the CdTe layer, with most recombination occurring in or near the depletion region of the junction.

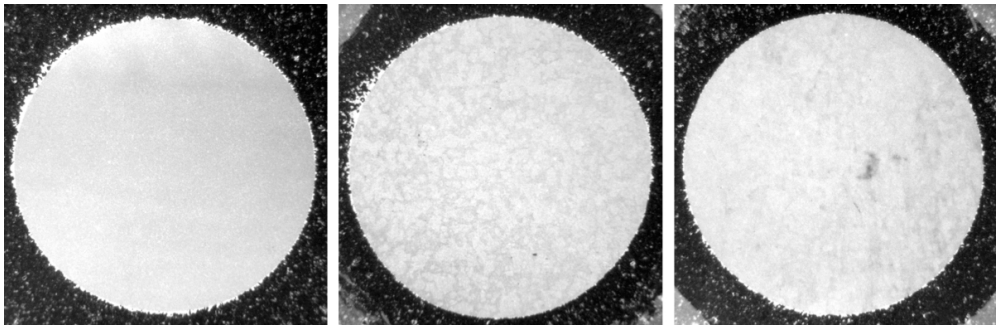

FIGURE 3.9. PL images of 9-mm-diameter CdTe solar cells showing a highly uniform PL signal (left), a sample which shows cleaning residue across the surface (middle), and a non-uniform cell containing both dark and bright spots (right).

PL signatures specific to CdTe include bright scratches, bright spots, dark spots and dark scratches. The majority of the bright spots are believed to be the result of reflection on the glass and TCO. The dark spots could be due to either optical blockage of signal between the glass, TCO, and bulk layers or a drop in radiative recombination due to resistive effects or current diversion. There are several examples of PL on CdTe that are seen in both Fig. 3.9 and Fig. 3.10. The first set of images shows PL signal with varying uniformity. The image to the far left shows a cell that gives off a very uniform PL signal. The middle image shows the dark pattern resulting in residue on the glass/TCO from the cleaning process. The image on the right shows a cell with various types of features, including dark spots and a small bright spot which appears to be increase recombination and not optical reflectance.

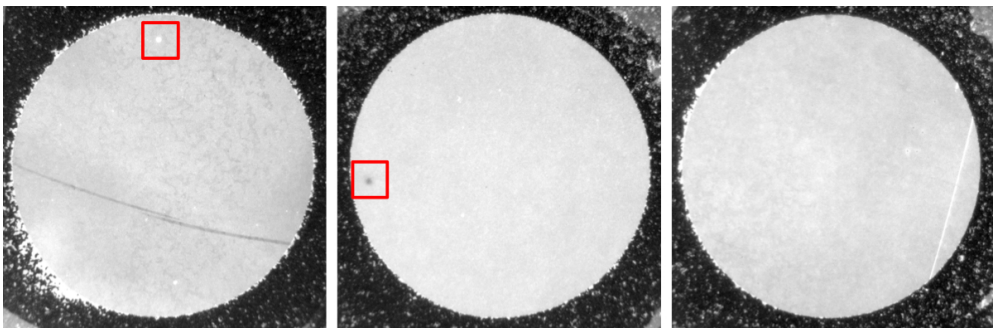

FIGURE 3.10. PL images of CdTe solar cells that have a bright spot (highlighted) and dark scratch (left), a dark spot as highlighted (middle), and bright scratch (right).

Fig. 3.10 shows the specific types of signatures mentioned above. The dark spots and scratches can be seen in the left and middle images. There is a very bright spot seen in the far left images and a bright scratch that appears in the bottom right side of the cell in the righthand image. The frequency of these types of features varied. The scratches, both bright and dark, were rare, although the dark scratches appeared more frequently. There were bright spots which appeared across devices in the same sets that were reflections from spots seen in room light; these did not appear to have a significant impact on cell performance.

PL imaging has the potential to save materials, energy, and time if it is successfully implemented during the manufacturing process. In an attempt to see how PL would fare as an in-line instrument for early material quality evaluation, unfinished CdTe devices were made and imaged using PL. The samples consisted of a set of films that were made at CSU with the heated-pocket deposition method with varying process conditions, beginning with an as-deposited CdS/CdTe film on a glass/TCO substrate. The subsequent films contained typical post-CdTe deposition treatments, each subsequent film processed more than the previous, including: TCO/CdS/CdTe with a $CdCl_2$ treatment, TCO/CdS/CdTe with $CdCl_2$ and Cu_1 treatments, TCO/CdS/CdTe with $CdCl_2$, Cu_1, and Cu_2 treatments, and one with all treatments and a high-temperature annealing. The PL signal of each film, both intensity and spatial variation, were compared to each other in order to see how processing steps affected PL. These images showed that PL is a quick diagnostic for unfinished CdTe solar cells. It not only shows the overall changes in signal, but small variations in the films that can eventually cause severe changes and variations that decrease cell performance.

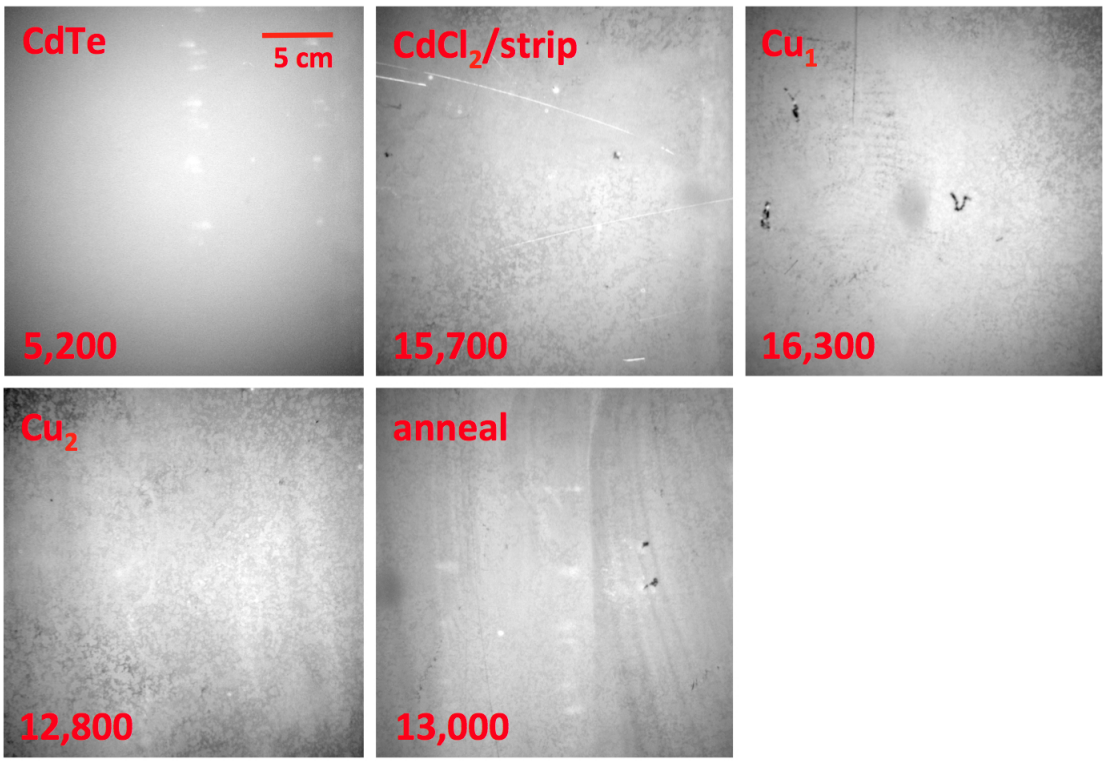

FIGURE 3.11. PL on CdTe post-deposition films with various processing steps (from left to right, top to bottom): no treatment, with $CdCl_2$, up to first Cu, up to second Cu, and through annealing. The average intensity is denoted in red for each of the films.

Imaging results included successful acquisition of PL images on all samples, as shown in Fig. 3.11. The intensity of the PL signal was very low for the TCO/CdS/CdTe film, but it greatly increased after the $CdCl_2$ treatment. The contrast was such that most features were more distinct and more detailed characteristics were easily seen after the $CdCl_2$ treatment, but spatial variations were seen in the as-deposited CdTe. The signal increased slightly after the first copper treatment (Cu_1), decreased by about 30% after the second copper treatment (CU_2), and then increased after the annealing process. Features that were detected as early as post-$CdCl_2$ treatment could be seen after the back contact was deposited and a full device was made. Each device, however, remained as-is before undergoing metallization. (No other post-deposition processes were completed on the devices between imaging the films and adding the back contact.) PL images of these films, along with average intensities, can be seen

in Fig. 3.11. This study did show that spatial variation and changes in luminescence could be detected by PL. This means that PL imaging could be used as an in-line evaluation tool, but further work would have to be done in order to correlate PL signal of unfinished films with final performance parameters to distinguish poor devices containing harmful defects from average and above-average devices.

3.4.2. Parameter Correlations. Linking luminescence to device parameters is highly dependent upon the cell type, differing among technologies and even different types of fabrications within a single type of device. As mentioned previously, Si performance was able to be quantitatively determined using PL imaging [21], while correlations between PL, EL, and device parameters were found in CIGS [7]. For CdTe, greater quantification of the PL signal and correlations of PL with device parameters would mean improving PL imaging as a characterization technique. Because of the complications with light sources and filters, the PL signal could not be quantified. One step toward improving this would be separating PL signal and reflected light. The two were not distinguishable with the available setup. But comparisons could be made, including comparing intensities and variations among samples made with identical processing conditions and seeing how varying processing steps affected the PL signal.

Work similar to that done in Chapter 2 to relate EL signal to device parameters was done with PL in order to study the relationship between cell quality and PL. Average PL intensity was determined using PL over an entire cell at 1 sun illumination. Device parameters such as J_{SC}, V_{OC}, fill factor, and efficiency were acquired using standard JV measurements. No correlations were found between PL signal and device parameters. If anything, a negative trend was found in the data, so that as V_{OC} and efficiency increased, PL signal decreased.

This was found for many types of devices that were well behaved (with efficiencies above 8% and no large shunting or resistive issues). These data were unlike that of Si and CIGS studies done at NREL, where there was a strong positive correlation between PL intensity, V_{OC}, J_{SC}, and efficiency [7]. Further work relating PL to EL is shown in a later chapter.

3.5. Conclusions

There were over 200 CdTe solar cells used to acquire nearly 1,300 PL images for this study. These data were one of the first of their kind showing room-temperature PL imaging on thin-film CdTe cells.

With the preliminary studies and the PL data taken on CdTe, there are limited qualitative data. What information that is provided by the imaging is limited by the reflected illumination source that is transmitted to the detector and cannot be separated from the PL signal. But spatial information can be acquired from CdTe devices, even on unfinished films, which is very advantageous for identifying potentially harmful inhomogeneities during production. PL signatures show nonuniformities, especially defects in the glass and TCO which cause reflection or signal blockage, as early as after the CdTe deposition. Variations in signal also indicate a change in performance and carrier generation after post-deposition treatments and annealing occur. The details and variations increase from the as-deposited CdTe films to after the first treatment ($CdCl_2$).

PL is expected to change with minority-carrier lifetime, which is related to short-circuit current density and other performance parameters. But no strong correlations were found between the PL intensity and J_{SC}, fill factor, and efficiency values. Studies on injection and carrier generation as related to PL did show a variation in the rate of change in PL intensity for excitation power greater than one sun. This crossover signified a change from

low injection to high injection in the CdTe devices. And increasing exposure times showed a linear increase in PL intensity, as expected.

Better illumination sources and filters that are more suited for CdTe carrier excitation, blocking reflected light, and collecting PL signal will help move towards quantification. Recognizing this deficiency, a solid foundation has been established for further work to build upon.

CHAPTER 4

Other Techniques

Along with EL and PL imaging, other characterization measurements were used in order to tell as complete a story as possible in regards to CdTe solar cells. Spectral photoluminescence (PL) and time-resolved photoluminescence (TRPL) are non-imaging PL techniques that quantitatively gather data on the emission spectra and lifetime of minority carriers, respectively, in solar cells. Dark lock-in thermography (DLIT) is another imaging technique that detects heat signatures given off by defects related to current crowding. Light-beam-induced-current (LBIC) measurements provided spatial quantum efficiency (QE) information. These four techniques are described below, along with the data and analysis for the CdTe solar cells

4.1. Spectral PL

While emphasis was placed on photoluminescence imaging, PL spectral emission data were also taken. CdTe has a room-temperature band gap near 1.48 eV (corresponding to a wavelength of 840 nm), which is the expected energy of band-to-band PL emitted from a CdTe cell. To quantitatively determine the spectra of the PL signal and confirm dominant near-band gap emissions, both room- and low-temperature spectral PL data were taken at NREL. PL spectral mapping was also done using a similar setup with a translational stage to construct spatial spectral plots for the cells. Data acquisition was straightforward, with analysis offering some insight into the physical details of PL emission.

4.1.1. Data Acquisition. The PL spectral mapping system used a 633-nm HeNe laser with a spot size on the order of 250 μm. PL emission spectra were acquired by scanning

the laser in the x and y directions over the surface of the cell. Measurements used 0.5-mm steps to scan the CdTe samples. The detector measured wavelengths from 650-1100 nm. Contour plots and two-dimensional intensity plots, which showed PL intensity as a function of wavelength, were then constructed for each wavelength.

Room-temperature and low-temperature spectral PL emission measurements used a 532-nm diode-pumped solid-state laser. The samples were placed in a closed-cycle He cryostat. The laser that was used to locally excite carriers had a spot size of about 100 μm. The emitted PL signal was then detected by a spectrometer with a 1024-by-1024-pixel Si CCD detector. Data were taken at 298 K and 9 K. The PL signal was carried towards the detector in the same fiber as the excitation laser and separated from the laser light using a beamsplitter. For this setup, reflection was not an issue like in the PL imaging. Another advantage that these measurements had over imaging was that the laser was monochromatic, so the excitation laser did not need as much power as in PL imaging.

Spectral EL measurements were also attempted after the PL spectra were acquired. A similar system to the spectral PL measurements was used, with the excitation laser replaced with a power supply in order to apply a bias to the cells. The EL signal, however, was too low for detection with the available setup. An amplifier, which was not available at the time, would likely be needed in order to detect a sufficient signal.

4.1.2. Analysis. Expectations for PL emission spectra included a large peak that arises around 1.48 eV, or 840 nm, which corresponds to the band gap energy of CdTe. One would also expect to see other peaks related to mid-band gap defect states and the presence of alloys related to CdS and CdTe. For PL spectra acquisition at 298 K, there was a dominant peak centered at 1.45 eV, or 855 nm, slightly below the band gap of CdTe. This main peak

had a large spread, with a full-width at half-maximum (FWHM) of over 100 meV. There was also a small peak present at 1.69 eV (735 nm), which could be from the CdS.

Lower temperature measurements are expected to decrease the FWHM. To resolve the peaks, the cryostat was cooled and measurements taken at 9 K. The resulting spectrum showed the dominant peak centered around 805 nm (corresponding to 1.54 eV, which matches the band gap of CdTe at low temperatures). The FWHM was reduced to about 65 meV. There was also a smaller peak at 1.59 eV that was not present in the room-temperature measurements that may be a result of mixed CdTeS near the junction. Finally, there was a peak at 1.39 eV that likely originated from defect states. The spectra for the room-temperature and low-temperature measurements are shown in Fig. 4.1.

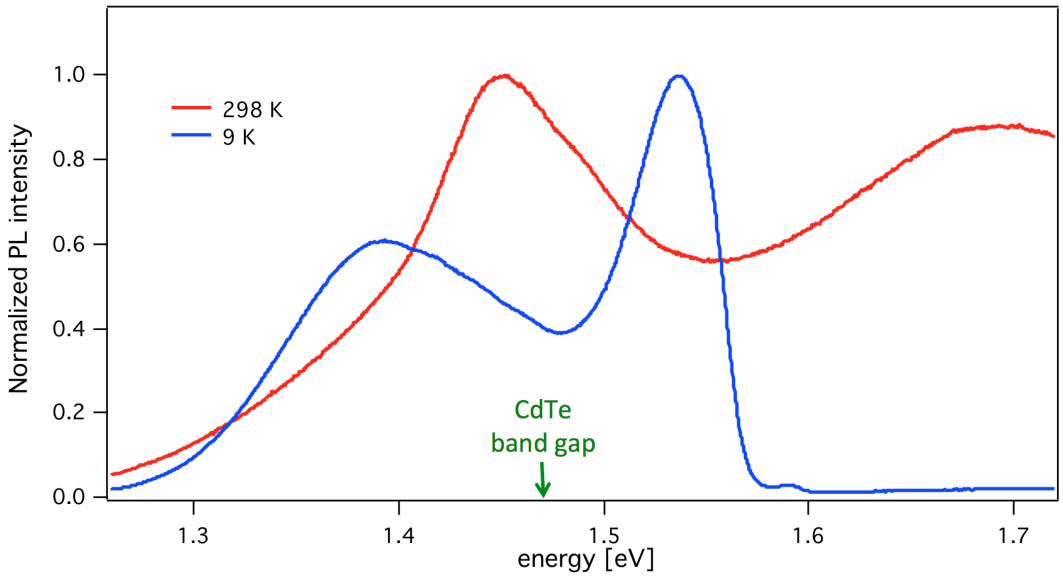

FIGURE 4.1. Room- and low-temperature PL emission spectra of a CdTe sample.

The mapping data showed a large intensity peak at 815 nm (1.52 eV) as a result of the CdTe band-to-band emission and a smaller peak at 1.35 eV that could be a result of Cu diffusion and other defect states. Contour maps for individual wavelength, which show PL

intensity values over the entire cell, were similar for each cell. The contour plots with the highest intensities were between 800 nm and 830 nm, as expected from the spectra.

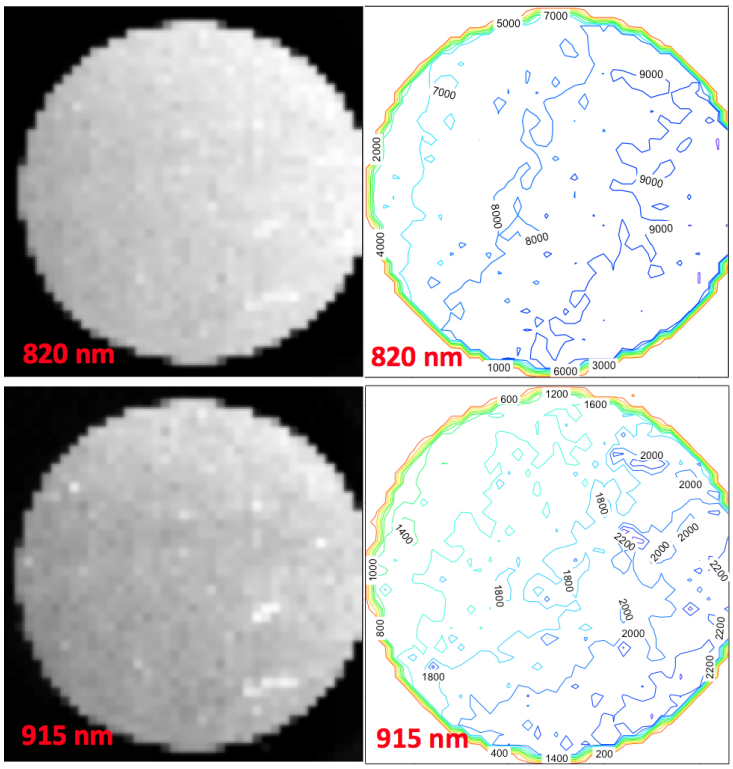

FIGURE 4.2. PL maps (left) of a 9-mm-diameter CdTe sample at two different wavelengths. The corresponding contour plots on the right show intensity delineations.

4.1.3. CdS SPECTRA. Additional PL spectral measurements were done on CdS films. The CdS, which is used as the window layer for CSU's CdTe solar cells, was modified by varying two of the processing steps: plasma-cleaning the glass substrate before deposition and adding a $CdCl_2$ treatment, which acted as an annealing step, after the CdS deposition. The spectral PL measurements were then used to study how these treatments affected the films.

Two different sets of CdS films were used. One set included the post-deposition $CdCl_2$ treatment and a control sample while the other set used the plasma cleaning and various CdS film thicknesses, ranging from 95 nm to 180 nm (typical CdS thickness is 120 nm). Room- and

low-temperature PL emission spectroscopy provided information on band-to-band emission and defect properties.

Results show that substrate preparation processes as well as CdS thicknesses affected the intensity of the PL signal. In particular, the post-deposition $CdCl_2$ treatment increased PL by more than a factor of two. The plasma cleaning also increased the PL intensity, although less so than for the $CdCl_2$ treatment. There was also no measurable variation in the near-band peak (of 2.4-2.5 eV) from sample to sample, even across sets. Furthermore, the 2.45 eV peak was the dominant one for both sets with a secondary sub-band gap peak at 2.15 eV for the $CdCl_2$-treated and a very small peak at 1.6 eV for the plasma-cleaned samples that increased as CdS thickness decreased. There were no systematic differences in the quantitative intensities of these peaks.

Low temperature measurements revealed a shift to lower energies for all peaks (as expected) and an increase in PL signal for the 2.1 eV peak in the $CdCl_2$-treated set as well as the appearance of a broad peak for the plasma set. This can be seen in Fig. 4.3, where room-temperature and low-temperature spectra from each set are plotted together. Low-temperature data of all samples showed that the PL signal of the annealed set was larger than the CSU plasma set by an order of magnitude. The broad peak also lies between 2.0 eV and 2.1 eV, varying from sample to sample.

4.2. TRPL

PL imaging provides qualitative spatial information for the effective minority carrier lifetime of the material in a solar cell. In order to acquire actual lifetimes for the CdTe samples, time-resolved photoluminescence (TRPL) measurements were performed at NREL. This technique extracts two lifetimes from a exponential fit of a histogram of photon counts

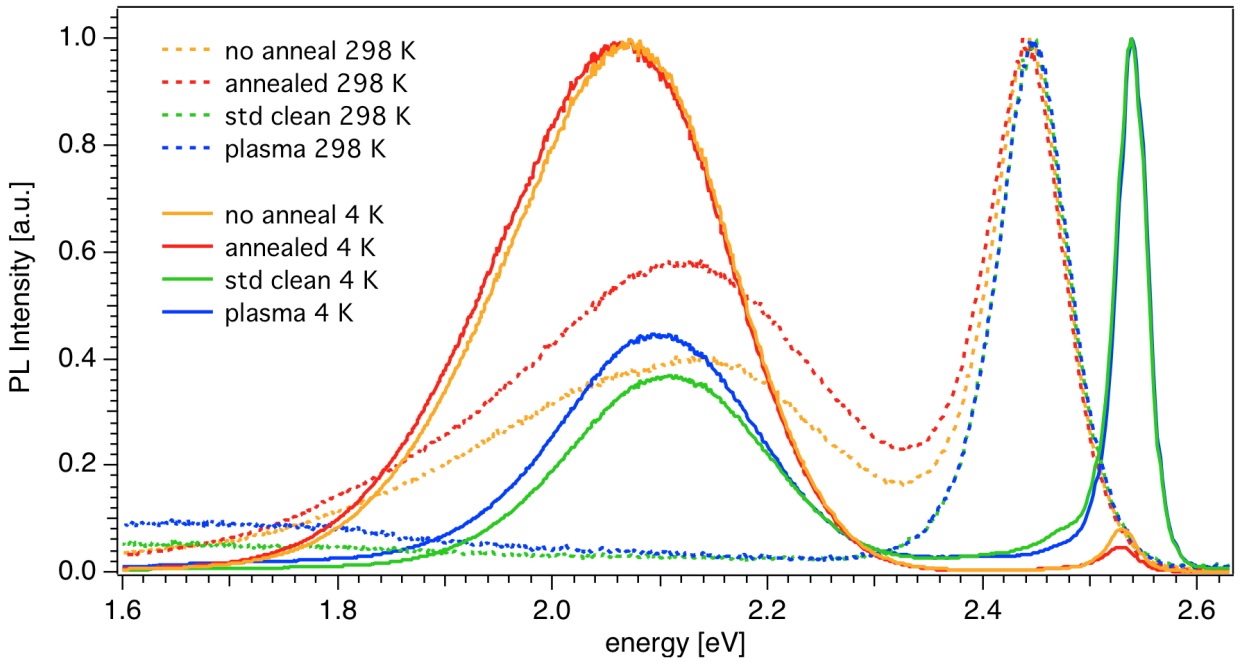

FIGURE 4.3. Room-temperature and low-temperature (4 K) PL spectra of two samples from each set of CdS films.

versus time that corresponds to PL decay [22]. The two lifetimes likely result from carrier recombination near the CdS/CdTe interface and in the bulk region, away from the interface.

The curves typically follow a two-exponential fit. The data are fitted to the following equation:

$$\text{Intensity} = \mathrm{A}_1 e^{-\frac{t}{\tau_1}} + \mathrm{A}_2 e^{-\frac{t}{\tau_2}}, \tag{9}$$

where A_1 and A_2 are the amplitudes.

4.2.1. DATA ACQUISITION. Measurements are done with a 1028-nm, 11-W laser that has a frequency of 1.1 MHz. which means it can deliver pulses on the order of 1 microjoule. The system uses an optical parametric amplifier, or OPA, that changes the 1028-nm photons into 516-nm photons with a series of crystals. There are 0.3-ps pulses every 0.5-1 μs.

Polarizers, beam splitters, mirrors, lenses, and neutral density filters are used to control the power and direct and focus the laser. A single-mode fiber brings the excitation beam to the sample. There is another fiber positioned after the beamsplitter that picks up PL emission and brings it to the monochrometer, PMT, and event counter. The acquisition time was set to 4 ps for these measurements. Monochrometer wavelength was set to the appropriate wavelength to look at CdTe. A basic schematic of the TRPL system is shown in Fig. 4.4.

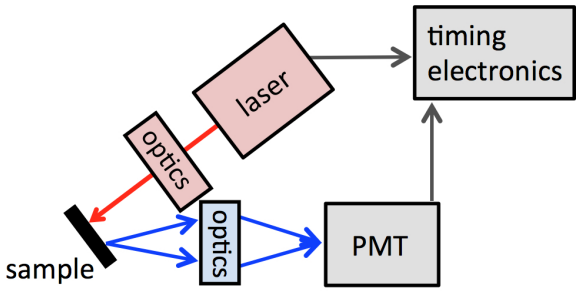

FIGURE 4.4. A basic schematic of the TRPL setup at NREL.

The data collected were histograms. With each single photon that is detected, there is a corresponding point on the plot of the PL intensity as a function of time. The time refers to the elapsed time between when the excitation laser fires and when the resulting photon is collected.

4.2.2. RESULTS AND ANALYSIS. TRPL measurements were done on different CdTe devices. The measurements were typically made on set of samples for comparison studies. Although the measurements were straightforward, the interpretation of the data is complex [20] and depends on the bulk lifetime, interfacial recombination, and the electric field distribution in the junction region.

Fig. 4.5 and Table 4.1 show the decay curves and corresponding lifetime values for three well-behaved CdTe samples. The lifetime values for the three sample are different within uncertainty, although cell efficiencies and lifetimes do not correlate.

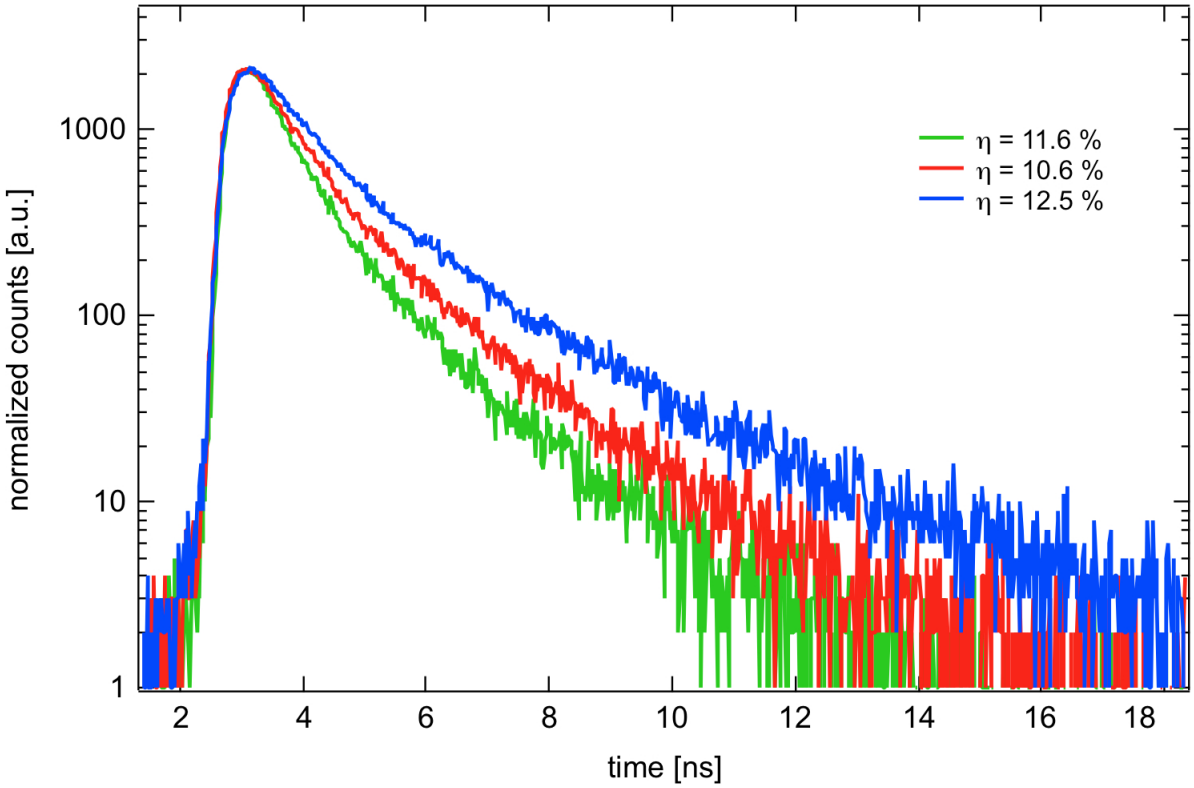

FIGURE 4.5. TRPL decay curves for three different CdTe samples (with sample efficiencies shown in the legend). The corresponding lifetime values extracted from these curves are shown in Table 4.1.

TABLE 4.1. Lifetime values for the TRPL decay curves shown in Fig. 4.5. Note that higher device efficiency does not correspond to higher lifetimes.

sample η [%]	τ_1 [ns]	τ_2 [ns]	τ_{avg} [ns]
10.6	0.72	1.8	1.0
11.9	0.60	1.7	0.8
12.5	0.76	2.1	1.3

4.2.3. CdS LIFETIMES. The $CdCl_2$-treated films discussed above were also measured using TRPL to determine minority carrier lifetime. The main focus was to see how the

treatments affects the films. An excitation wavelength of 440 nm, suitable for the 2.4 eV band gap of CdS, was used as an excitation source.

Results show the set having a two-exponential decay with $\tau_1 = 0.5$ ns and $\tau_2 = 2$ ns for the as-deposited film and τ_2 increasing to 3 ns after the $CdCl_2$ treatment. τ_1 was uneffected. These values, as seen in Table 4.2 were extracted from the decay curves also shown in Fig. 4.6. There was also a correlation between longer lifetimes and stronger PL emission signals as seen in the TRPL measurements. This increase in signal, along with the higher lifetimes in TRPL, show that annealing leads to an increase in material quality.

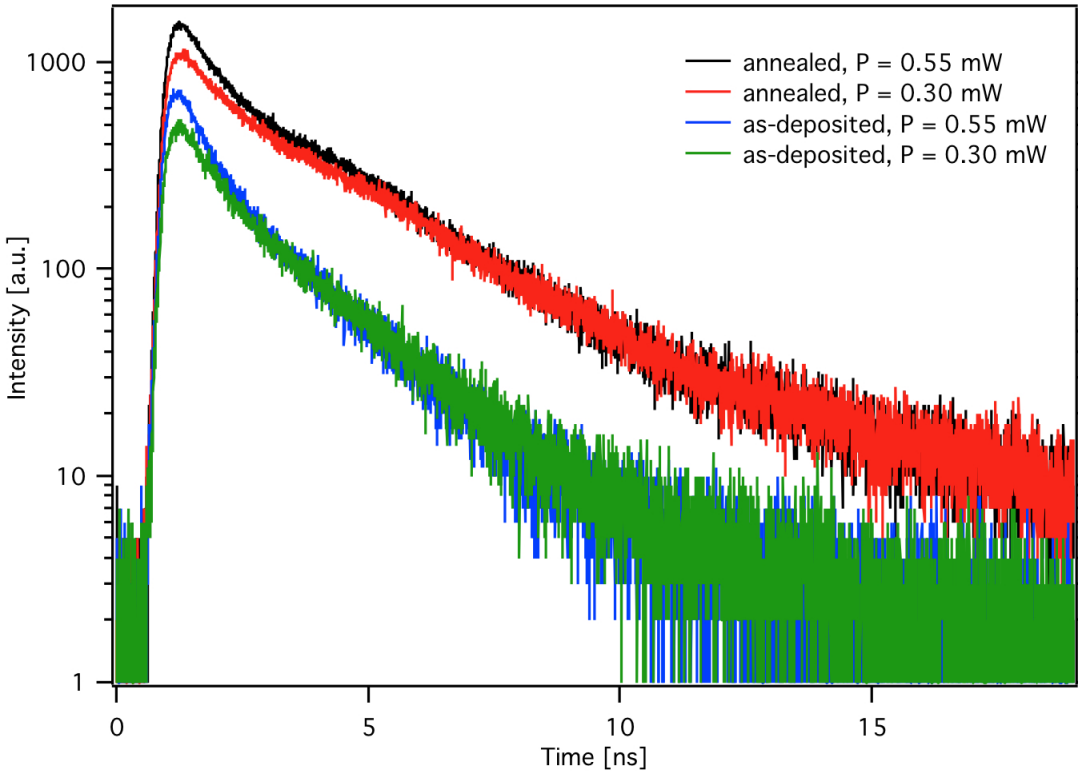

FIGURE 4.6. TRPL decay curves for the two CdS films (as-deposited and annealed).

TABLE 4.2. Lifetime values for the CdS film TRPL decay curves shown in Fig. 4.6.

sample	laser power	τ_1 [ns]	τ_2 [ns]
as-deposited	0.30 mW	0.54	2.2
as-deposited	0.55 mW	0.49	2.0
annealed	0.30 mW	0.48	3.0
annealed	0.55 mW	0.44	2.8

4.3. Dark Lock-in Thermography

Dark lock-in thermography, or DLIT, uses an infrared detector to image thermal signatures in solar cells placed under bias via periodic voltages, both forward and reverse. The current flow through a cell under bias results in an increase in temperature from Joule heating. A solar cell under forward bias has current flowing through the entire device, provided it has no severe defects, with the entire cell rising in temperature. This thermal signal will then produce an image. Reverse bias allows for the detection of shunts and other current-crowding effects. There is typically only a small current flowing through a device at reverse bias, but shunts and other defect regions can cause paths for larger currents. These regions are enhanced by reverse-bias avalanche breakdown [19]. Different types of defects have different signatures. This study includes a catalogue of thermography signatures seen in CdTe cells and works to identify the origins and physical explanations of these signatures.

4.3.1. Data Acquisition.

DLIT images were acquired using an InSb infrared camera from FLIR/Cedip with a 640 pixel × 512 pixel grid and built-in lock-in detection. The maximum field-of-view with the built-in lens is 305 mm × 245 mm, corresponding to a resolution of 477 μm/pixel. With the use of other lenses, the camera provides very high resolution with a field-of-view down to 2.4 mm × 1.9 mm, or 3.7 μm/pixel.

The lock-in data acquisition mode increases the sensitivity of the camera by building an amplitude and phase image using a pulsed signal from a function generator to bias the cell. The bias voltage and the camera's lock-in electronics were set to acquire frames at a frequency of 6.7 Hz, which provided the best signal resolution for the CdTe samples. Although solar cells are typically imaged from the front side, the front glass of the CSU CdTe devices blocked the heat and no signal was detected through the front. So the devices were flipped and the image acquired through the back metal contact. This thick metal layer dissipated the heat but transmitted a signal, unlike the 3-mm thick front glass.

Bias values had to be kept low because high voltage, especially in reverse bias, may have damaged the cells. When a large current is forced into one area and the cell heats up considerably, there may be permanent changes to the structure that affect cell performance. Forward biases ranged from 0.5-1.2 V. This produced currents up to 20 mA, similar to typical J_{SC}. Reverse bias values ranged from 1-4 V, depending on defect presence and severity. Both forward and reverse biased images were taken of each sample being measured.

Signatures seen in DLIT of CdTe include hot spots varying in size that appear in the cell center or on the edges. There are also gradients in thermal signal along the width of the cell. Few scratches were seen, but they did occur. There were also dark regions, either in the form of concentrated spots or lines spanning the cell. Example of different features are shown in Fig. 4.7.

As seen in the example images in Fig. 4.7, there is a distinct difference between forward- and reverse-bias images. Forward-bias images show a mostly uniform heating over the entire area of the cell, signifying current flow throughout the device. There are some bright and dark areas, signifying current crowding and lack of current, respectively, as well as gradients.

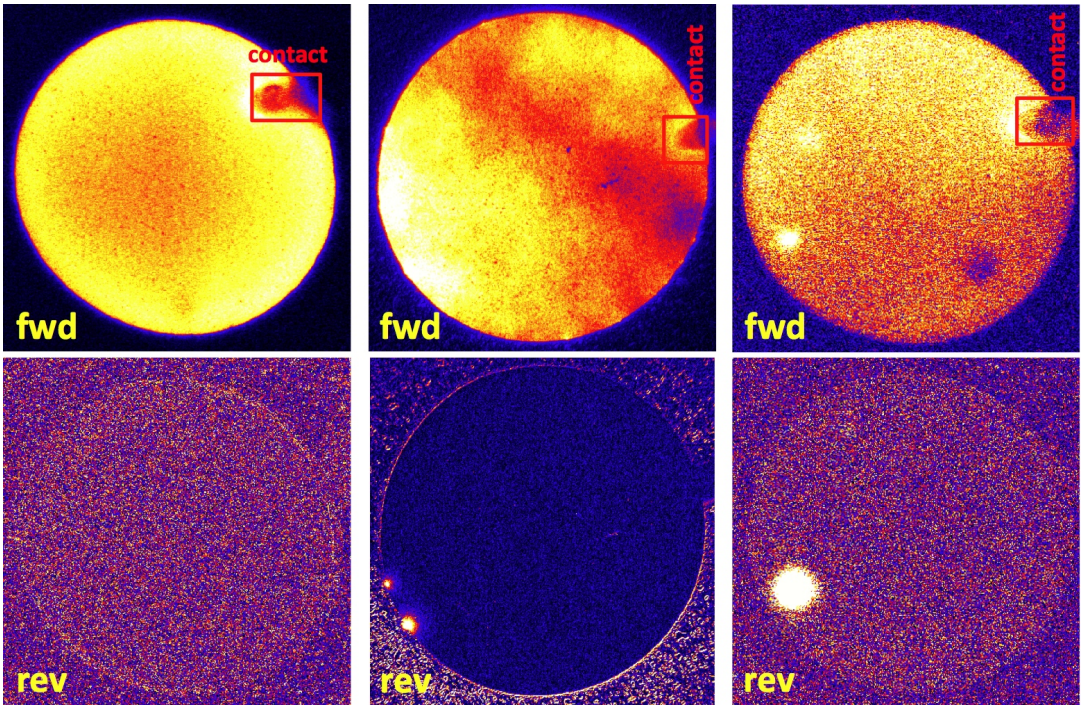

FIGURE 4.7. DLIT images of three 9-mm-diameter CdTe solar cells with various signatures. The forward-bias images are shown in the top, while the corresponding reverse-bias images are shown on the bottom. The dark spot in the upper right corner of each of the samples is the contact probe.

The hot spots, or local bright spots, were of particular interest in this study because of their potential for being shunts and weak diodes.

Shunts, weak diodes, and other defects appearing in CIGS were identified and imaged using DLIT at NREL, and their signatures were linked to physical causes. This had not yet been done with CdTe but defects in the two technologies were assumed to be closely related. This previous knowledge of CIGS was used to study DLIT features in CdTe. Most of the 200 samples imaged with EL and PL were also measured using DLIT, with close to 1,000 images collected.

4.3.2. ANALYSIS. The severity and frequency of the hot spots varied. There were also some that appeared in forward bias, some in reverse bias only, and some in both. About half of the cells had edge features that appeared in reverse bias, and a smaller number in forward

bias. They also tended to affect a larger area in reverse bias. As seen in Fig. 4.8, because in forward bias, more of the total current is flowing through the entire cell, whereas in reverse bias the defect draws most of the current because it has a lower breakdown voltage than non-defect areas.

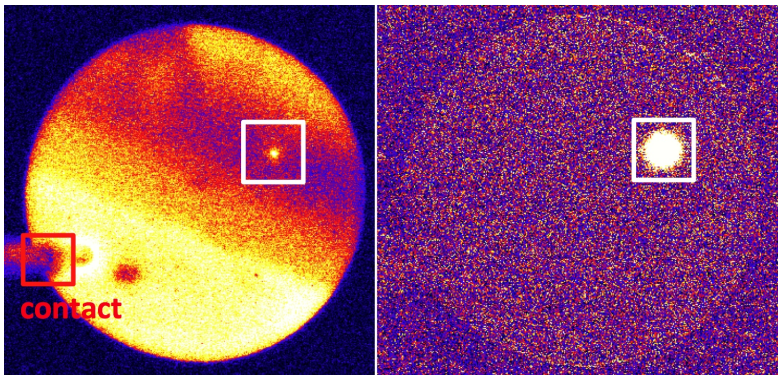

FIGURE 4.8. DLIT images showing a feature in a CdTe cell that is seen in both forward bias (left) and reverse bias (right). The feature affects a greater area and is more pronounced in reverse bias than in forward bias.

Hot spots within the cells appeared in less than 10% of the samples. This may be because defects which occurred in the cell's center, where the materials are nominally disrupted, were not very common. It may have also been that the edge effects were much more severe than in the middle so that most of the current was directed towards the edges.

To begin to identify the physical origins of the hot spots, a comparison was made with CIGS data. Shunted areas appear as bright spots in reverse bias and not in forward bias for CIGS. Weak-diode areas appear bright in both forward and reverse bias [7]. And for CIGS, forward-bias DLIT was sensitive to series resistance in the TCO layer [19]. This was the starting point that was used to help distinguish between shunts and weak-diode areas for CdTe.

DLIT on CdTe was more challenging than other technologies because the supersaturate configuration made thermal imaging through the front glass not possible. But because the

imaging was done through the back contact, the heat signatures were somewhat dissipated through the thick metal contact. Because of this limitation, thermoreflectance, another form of thermal imaging, was tried on the CdTe samples. Thermoreflectance, which uses lock-in data acquisition to detect changes in reflectivity, allowed high resolution imaging of defects through the front glass. A defect identified by DLIT and believed to be a shunt was successfully imaged. The resulting data showed far more spatial resolution than DLIT, with the thermoreflectance image showing a 20 μm $\times$ 40 μm defect with the heat concentrated at the center, in a 100 μm^2 area [23].

Connections were also made between EL and DLIT images, with more analysis presented in the proceeding chapter. This was done in hopes of identifying and studying shunted areas as they appear in EL imaging.

4.4. Light-beam-induced Current

Light-beam-induced-current measurements, or LBIC, provide a spatial quantum efficiency (QE) map of a solar cell. The LBIC measurements for this study were done at CSU, where a system was custom built for thin-film solar cells [24]. The laser diode enters a single-mode fiber and is directed onto the stage area after being passed through an attenuator to control the output power, a beam splitter, polarizer, and other focusing and monitoring optics. The laser spot hits the sample and excites only a small portion of the cell (1-100 μm, depending on the resolution of the scan). The output current is sent to a preamplifier, which converts the signal to a voltage, which is then measured with a lock-in amplifier. The output of the system is a map of apparent QE. A simple schematic showing the LBIC setup at CSU is shown in Fig. 4.9.

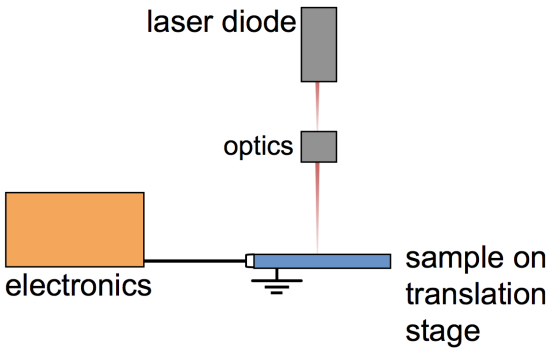

FIGURE 4.9. A simple LBIC schematic. The optics consist of focusing mirrors and lenses as well as equipment to control and monitor the laser output. The electronics are a preamplifier and lock-in amplifier.

4.4.1. DATA ACQUISITION. Samples were measured using a single-wavelength excitation of 638 nm. The laser spot size and power can be adjusted to perform scans with different resolutions. Initial measurements are usually made using low-resolution scans, which use a 100-μm spot and 50-μm step size, to acquired a large amount of information in a reasonable amount of time. (An entire 0.7 cm^2 CdTe sample took about four hours to measure using low-resolution measurements.) The x-y translation stage and coupled software allows one to focus in on regions of interest (usually a small feature seen in the initial scans) and perform a higher-resolution measurement. Mid-resolution scans use a 10-μm spot size and 5-μm step size. High-resolution scans use a 1-μm spot and 0.5-μm step size to zoom in even further. Initial measurements were performed at a 0 V bias. The amplifier applied a bias to the samples in order to keep the system in equilibrium, but an additional bias could be placed on the samples for additional measurements. Both forward- and reverse-bias LBIC scans were acquired on several CdTe cells to study the resulting effects.

4.4.2. ANALYSIS. Low-resolution scans showed typical QE values ranging from 80 to 90% for well-behaved cells. There were occasional large gradients across devices, although they did not appear very often. Other inhomogeneities appeared in the form of small spots.

These local drops in QE were typically 200-500 μm in diameter when they appeared in the low-resolution scans. Examples of these are shown in Fig. 4.10.

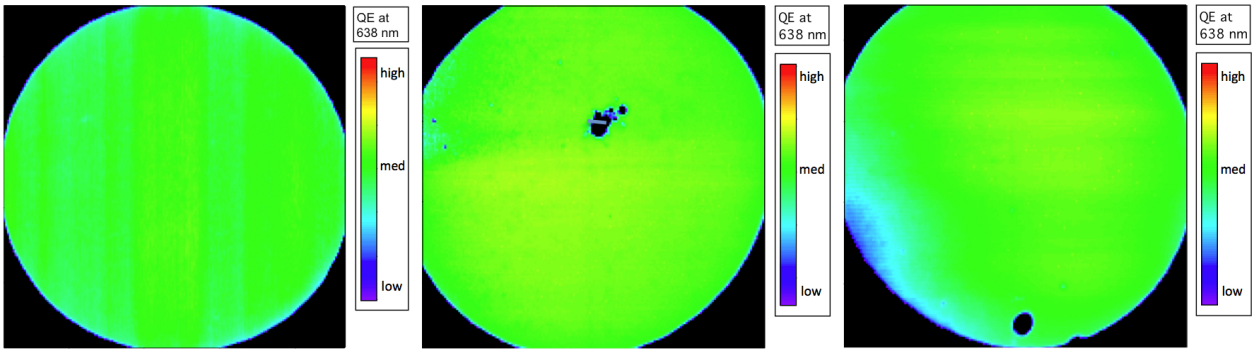

FIGURE 4.10. Low-resolution LBIC scans from three well-behaved 9-mm-diameter CdTe samples.

In addition to LBIC measurements done with no bias, forward- and reverse-bias measurements were also taken. There was often a significant difference between the different biases. The most common change was that decreases in local QE were much larger in forward bias. The reverse-bias maps were typically identical to 0 V scans. There were a few that showed even fewer inhomogeneities. This is a result of the masking of resistance features, especially in the TCO, when the cell is unbiased or in reverse bias. The built-in field also changes when the cell is biased, which affects carrier collection. Effects of different biases are seen in Fig. 4.11. Side-by-side comparisons are made between a cell in forward bias and no bias as well as between forward and reverse. A study done at CSU, which shows similar results to those presented here, also looks at the wavelength dependence (as well as bias dependence) on CdTe solar cells [25].

Mid- and high-resolution scans reveal much more variation throughout the regions of interest than their low-resolution counterparts, implying features that cause QE to drop are typically smaller than the 100-μm laser spot. An example of a region that appeared very

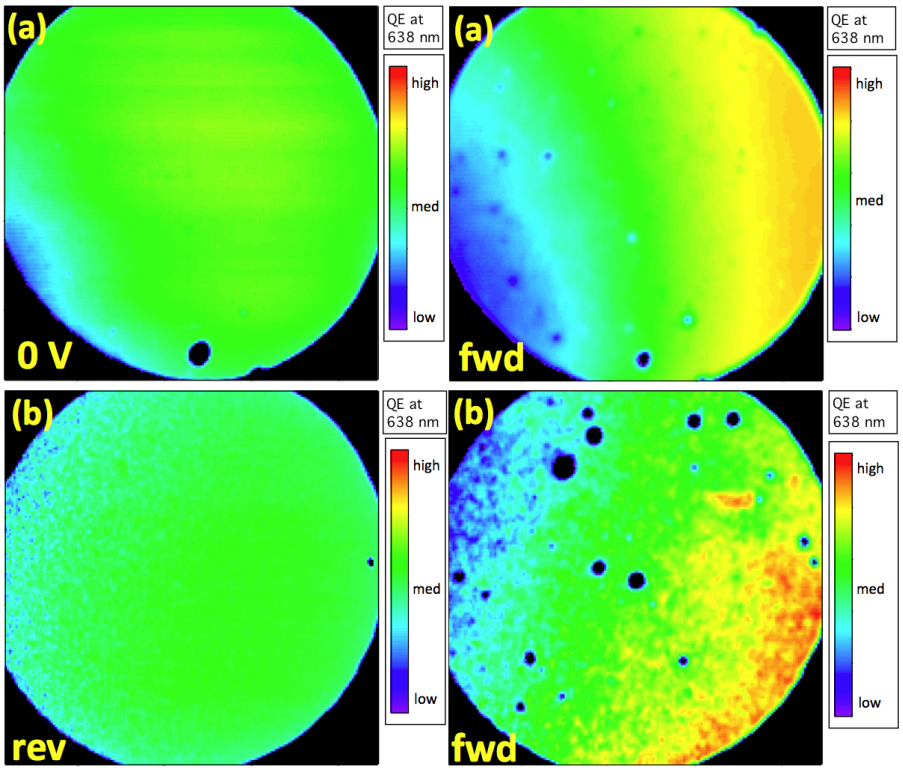

FIGURE 4.11. Forward-bias LBIC contrasted with 0 V bias and reverse-bias scans from two different CdTe samples.

uniform in an unbiased low-resolution scan contained much more variation in QE as seen in higher-resolution scans is shown in Fig. 4.12.

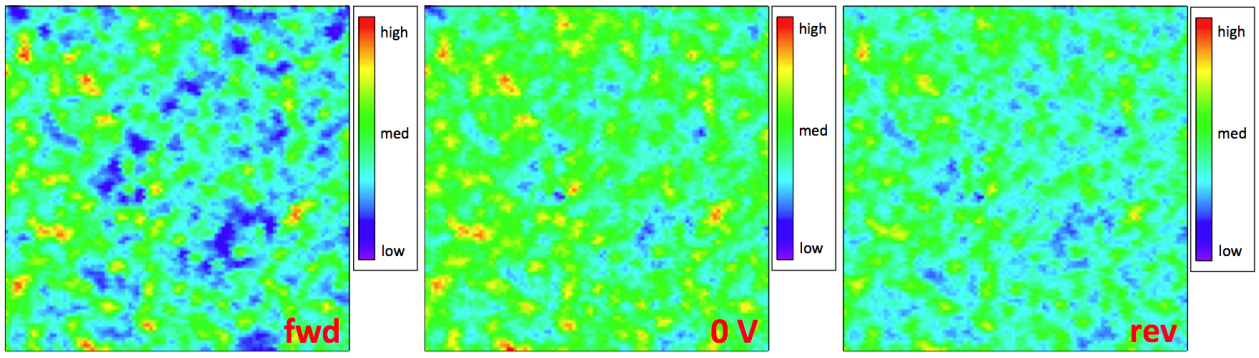

FIGURE 4.12. 500 μm $\times$ 500 μm mid-resolution LBIC measurements of a region of a CdTe solar cell that was fairly uniform in low-resolution.

4.5. Conclusions

In addition to electroluminescence and photoluminescence imaging, four other measurement techniques, all pretty common methods of characterization (more so in laboratories than during in-line manufacturing), were used to characterize CdTe solar cells. Each provided varying degrees of useful information, ranging from qualitative and spatial to quantitative and local.

Spectral PL, using a spectrometer to measure PL emissions, provided spectral data at low and room temperatures. At room temperature, 298 K, there was a dominant peak with somewhat of an offshoot corresponding to near-band gap emission at 1.45 eV which shifted to higher energies at 9 K. There was also a weaker peak at 1.7 eV most likely resulting from CdS/CdTe alloys that moved out of the range of the detector at 9 K. The spectra at 9 K revealed a very small peak which was separated from the dominant peak as a result of the low temperature. A broad, smaller peak at 1.38 eV also arose, likely due to mid-gap defects.

Time-resolved PL, or TRPL, provided minority-carrier lifetimes. There are two values extracted from decay curves that are related to the junction (τ_1) and the bulk (τ_2). Data showed that well-behaved devices with efficiencies around 10% produced lifetime values of 0.5-0.8 ns for τ_1, and around 2 ns for τ_2. These values are around the average values reported for CdTe solar cells. Measurements on CdS films showed similar values for τ_1 and an increase from 2 ns to 3 ns for τ_2 after the films were treated with $CdCl_2$. These CdS lifetime data are some of the only results reported thus far.

Dark lock-in thermography (DLIT) imaging revealed hot spots resulting from increased current flow in local areas of a device. Forward-bias measurements generally showed current flow through the entire device, with local bright spots occasionally arising mid-cell or around

the edges. Reverse-bias images revealed many more bright spots, most of which were around the edges, likely resulting from shunted regions.

Lastly, light-beam-induced current (LBIC) gave maps of the apparent quantum efficiency (QE). Local inhomogeneities could be seen in the constructed scans, with more local variation occurring in the mid- and high-resolution scans. There was also more overall variance and local drops in QE at forward bias than reverse bias and no bias.

In the following chapter, these measurements will be used to compare CdTe samples, and identify inhomogeneities and link them to cell performance more wholly for thin-film CdTe devices.

CHAPTER 5

Integration of Techniques

The integration of characterization techniques, particularly EL and PL, but in some cases other techniques, yields greater information than the techniques individually. Integrating the data began with comparing EL and PL signals to CdTe device performance, direct comparisons between spatial measurements, and finding the correlations. Similar work was done with CIGS, where a strong correlation was found between luminescence signal (EL and PL) and device parameters, particularly open-circuit voltage, V_{OC} [7]. Relating PL data with device parameters was also done with multicrystalline Si, using a series of five PL images to extract current, voltage, fill factor, efficiency, series resistance, and dark saturation current density [21].

For CdTe, direct comparisons included looking at overlapping features in EL and PL; DLIT aided in identifying shunts and edge effects which were initially catalogued in EL. Quantum efficiency (QE) maps acquired through LBIC and minority-carrier lifetimes extracted from time-resolved PL data were used as quantitative comparisons and to aid in identifying physical causes and effects of nonuniformities. This provided a comprehensive look into inhomogeneities arising in CdTe solar cells.

5.1. Comparisons

Table 5.1 lists overlapping features between the various techniques. This allowed for a direct comparison between techniques and identifying and describing inhomogeneities. Spatially, however, feature commonalities do not occur very frequently. As seen earlier, EL

TABLE 5.1. List of imaging and characterization measurements along with feature descriptions seen in each. A description of how the specified signatures appear in other measurements is also given to provide a good reference for technique integration.

EL		
feature	**responds to bias?**	**overlap with other techniques**
bright spot (interior)	yes - intensity	PL - bright spot or no feature
bright spot (edge)	yes - intensity	DLIT(fwd) - bright spot
dark spot	no change	PL - dark spot, bright spot, or no feature, DLIT(fwd) - hot spot or no feature, DLIT(rev) - hot spot or no feature
dark scratch	no change	PL - bright, dark, or no feature
bright scratch	no change	PL - bright scratch
gradient	slight changes	PL - similar variations or no feature, DLIT(fwd) - similar

PL		
feature	**responds to bias?**	**overlap with other techniques**
bright spot (interior)	no	EL - dark spot or no feature
dark spot	no	EL - dark spot (usually more contrast)
bright scratch	no change	EL - dark or bright scratch
dark scratch	no change	EL - dark scratch, DLIT(fwd) - gradient

DLIT(fwd)		
feature	**responds to bias?**	**overlap with other techniques**
bright spot	yes - intensity	DLIT(rev) - bright spot or no feature
gradient	some intensity changes	EL - gradient

DLIT(rev)		
feature	**responds to bias?**	**overlap with other techniques**
bright spot (interior)	yes - different turn-on voltages	EL dark or none
bright spot (edge)	yes - different turn-on voltages	EL - bright spots on edge

LBIC		
feature	**responds to bias?**	**overlap with other techniques**
local drop in QE	yes - frequency of features increase, size sometimes increases	EL - dark spots
large gradient	yes	EL - gradient, DLIT(fwd) - gradient

shows more inhomogeneities, usually in the form of decreased luminescence. PL, on the other hand, often shows features that arise from reflection.

A direct comparison between techniques allowed for identifying inhomogeneities and describing their appearance, size, and behavior in each technique.

Each technique has advantages, with the greatest seeming to be that PL can be implemented early on in the manufacturing process. Because of this advantage, PL has been studied extensively on mc-Si and other technologies. This has included using PL to image mc-Si from the initial brick to a finished wafer in order to study the effect of each processing step [16], [26]. It was also used on CIGS films to study effects of In/Ga grading and doping [7].

5.2. EL and PL

When making side-by-side comparisons between techniques, Si and CIGS have a high degree of feature overlap and CdTe does not. Fig. 5.1 is a good example of this, showing EL and PL images for the three different PV materials explored throughout this work: Si, CIGS, and CdTe. When directly comparing EL and PL images for CdTe, there are many differences in inhomogeneity signatures that appear in the two techniques. EL images display more detail than their PL counterparts in the transparent conductive oxide (TCO) layer. Inhomogeneities from cleaning residue and handling of the glass substrate prior to deposition appear as distinct, dark patterns in EL. There are also distinct PL signatures that arise due to the external illumination sources and reflection of the light in the 3-mm-thick glass substrate.

Features which do overlap include large signal gradients arising from compositional nonuniformities in the materials. Scratches on the glass superstrate were bright in PL because of reflection, but dark in EL because the scratch obstructed the signal. This also occurred with foreign material on the glass/TCO before material deposition; the particles

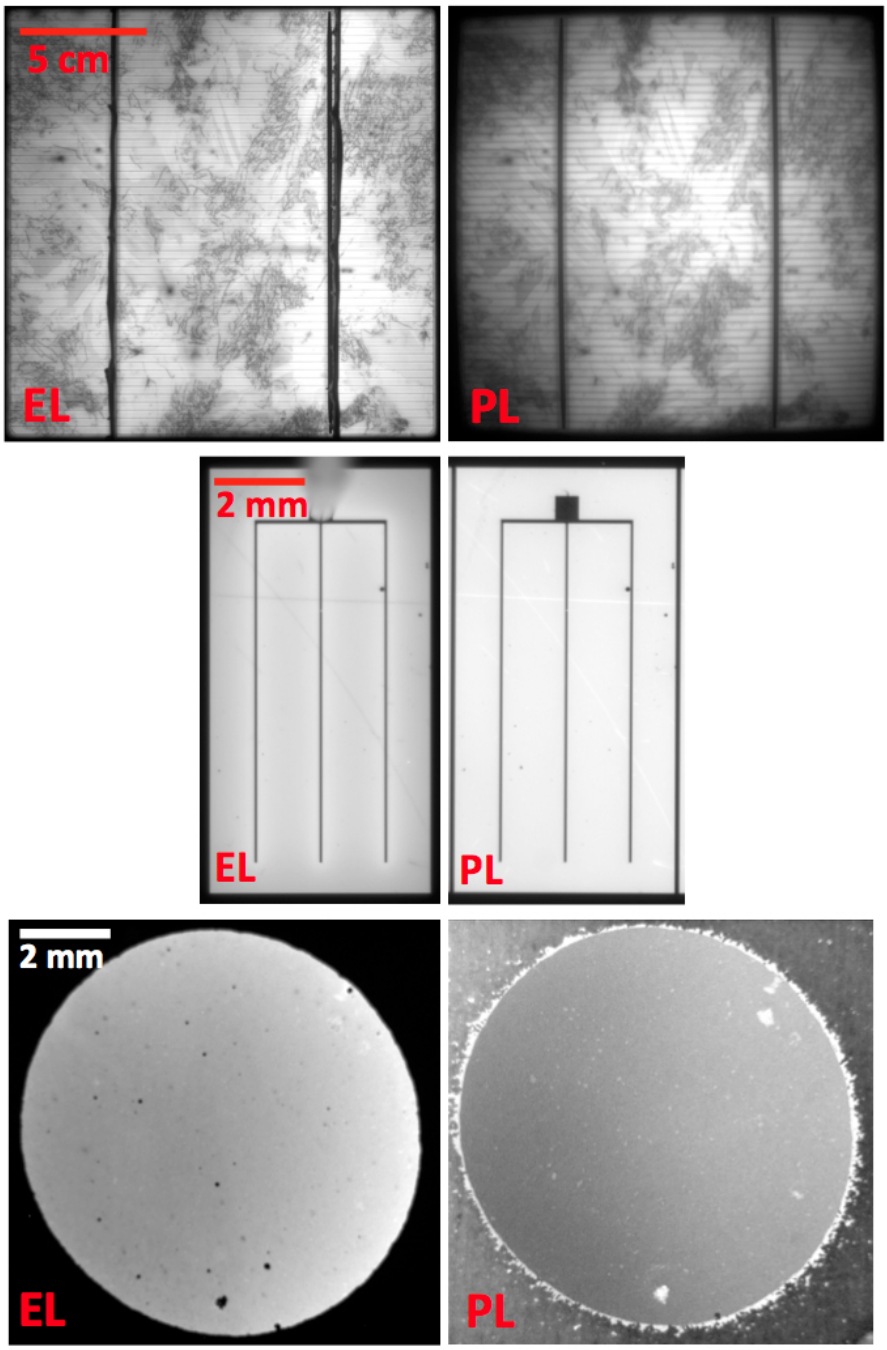

FIGURE 5.1. EL and PL images of Si (top), CIGS (middle), and CdTe (bottom) solar cells. The contrast between the center and edges of the PL image of Si comes from nonuniform illumination from the excitation laser.

reflected the external illumination source used in PL, showing up as brighter regions in the image, and acted as optical obstructions in EL images.

There are certain signatures that take precedence during analysis–those caused by defects such as shunts and weak diodes, which are detrimental to device performance. The signatures linked to these defects occurred less frequently. This was most likely because the majority of shunts and other defects that appear in modules are related to cell delineation and therefore occur most often at cell edges. A more detailed explanation of this is provided later.

For weak diode areas caused by thin cadmium sulfide (CdS), there is expected to be an increase in current, but lack of radiative recombination in that region creates dark spots in EL and PL images. The effect on local voltage, however, is unknown. If the weak diode causes the voltage directly around the defect to decrease but the surrounding voltage to increase, the EL signature would consist of a dark spot surrounded by a region with increased luminescence. This was not seen in data acquired for this study. Shunts also cause current crowding, decrease the local voltage surrounding the defect, and prohibit radiative recombination. Dark signatures are consistent with results in CIGS, where shunts and weak diodes are manifested as dark local regions in both EL and PL [7]. Other dark regions may occur if a large number of defect states exist in a particular region. The current crowding resulting from these defect areas also cause thermal signatures, which is discussed below.

5.3. Thermal Signatures

5.3.1. Defect Detection. Additional integration included the use of DLIT data to refine the interpretation of EL and PL data. DLIT is not a measure of luminescence but a very helpful imaging tool used to detect current flow and heat signatures from defects. Typical forward-bias DLIT images showed overall current flow in the CdTe devices and variations in current due to compositional non-uniformity by detecting thermal signatures

with a highly sensitive IR camera. These variations corresponded well with signal gradients in EL.

Conversely, reverse-bias DLIT revealed local hot spots due to increased current from defects. Many of these hot spots were located on the edges of the samples. A few of these thermal signatures were also present in forward bias, indicating a severe shunt. The hot spots like those in Fig. 5.2 that were seen in forward bias and not in reverse may have been a result of weak-diode behavior, which is consistent with DLIT signatures for CIGS, where features in DLIT that form because of breakdown junctions, shunts, or weak diodes correspond to dark regions in EL and PL [7]. When these signatures were located on the cells' edges, corresponding and consistent PL and EL signatures were difficult to find. But features that were located inside the cell typically corresponded to dark spots in EL and dark spot or no visible signature in PL, as noted in Table 5.1.

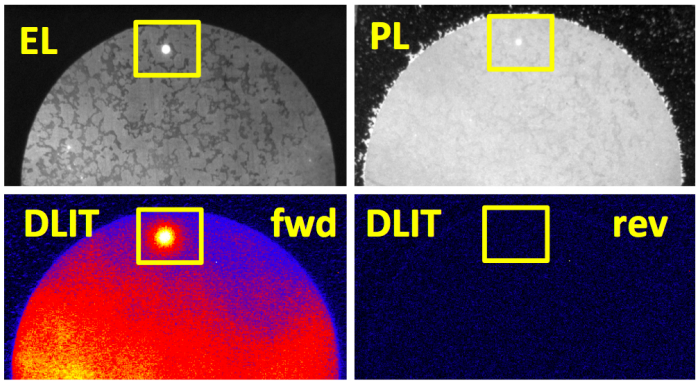

FIGURE 5.2. EL, PL, and forward- and reverse-bias DLIT images highlighting a defect region that exhibits weak diode behavior in a 9-mm-diameter CdTe cell.

Areas in solar cells that exhibit weak diode behavior resulting from a thin window layer cause leakage current from the absorber directly into the transparent-conducting oxide (TCO) and can cause current flow at smaller-than-average voltages, explaining the thermal signatures in forward-bias DLIT. These weak-diode defect regions decrease the overall power

output of a cell, and so are expected to decrease the overall luminescence intensity for a device. Shunts form a leakage current, dissipating power and affecting the voltage distribution. Because EL is related to voltage, the decrease in voltage caused by a shunt will be reflected as a decrease in EL signal, as seen in Fig. 5.3. This effect, as well as the effect of weak-diode regions and other defects on luminescence, was studied using modeling [9], [10], [17] and imaging data acquired on CIGS modules [9]. These results were used to help identify shunts and weak diodes in EL and PL images of CSU's CdTe cells. The majority of the data analyzed to help identify the physical causes of defect signatures was EL, since PL images of CdTe contained large amounts of reflected light along with the luminescence.

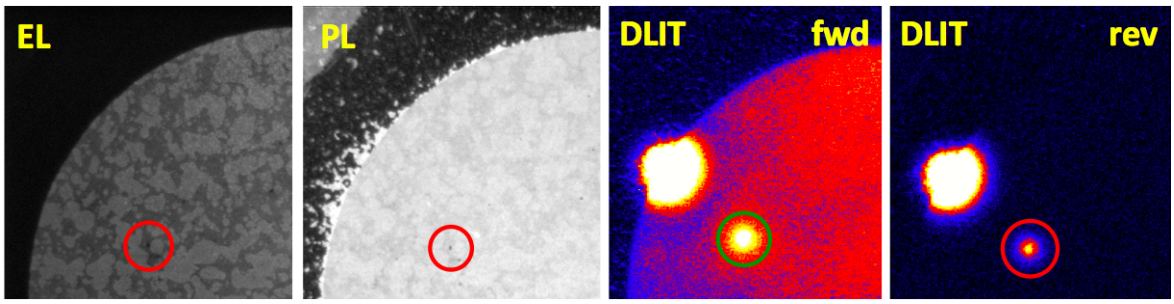

FIGURE 5.3. EL, PL, and forward- and reverse-bias DLIT images showing a shunt-like defect seen in a CdTe solar cell. The heat signatures in DLIT correspond to small dark spots in both EL and PL.

A thin-film heterojunction solar cell model can be created using a simple equivalent-circuit model composed of a diode array, with shunt- and series-resistance effects inserted into the circuit using resistors. The presence of shunt resistance causes a decrease in local V_{OC} with the radius of the affected area dependent upon the severity of the shunt. The shunt affects a larger area when there is less current flowing through the cell because the conductivity of a typical diode increases exponentially and the shunt conductivity stays constant. As applied to CIGS modules, it was determined that the majority of the luminescence features seen are due to resistive effects (related to series resistance or shunt defects) [9], [27].

The EL features that were studied were identified using heat signatures seen in reverse-bias DLIT. These were seen as local dark regions in the EL images. A series of images taken at different voltage biases showed that the EL signal distribution surrounding the defect did not vary (in area) with the voltage bias, as shown in the models and imaging data taken on CIGS modules. This behavior can be seen in the dark EL feature analyzed in Fig. 2.14.

5.3.2. Egde Effects. Because very few heat signatures were seen in the interior of the CdTe cells, it was suspected that the edge effects like the one seen in Fig. 5.4 dominated the interior shunt and weak diode areas, masking their DLIT signatures. The heat signatures in DLIT that did correspond to features in luminescence images were typically in the form of dark spots in EL and rarely corresponded to bright or dark spots in PL.

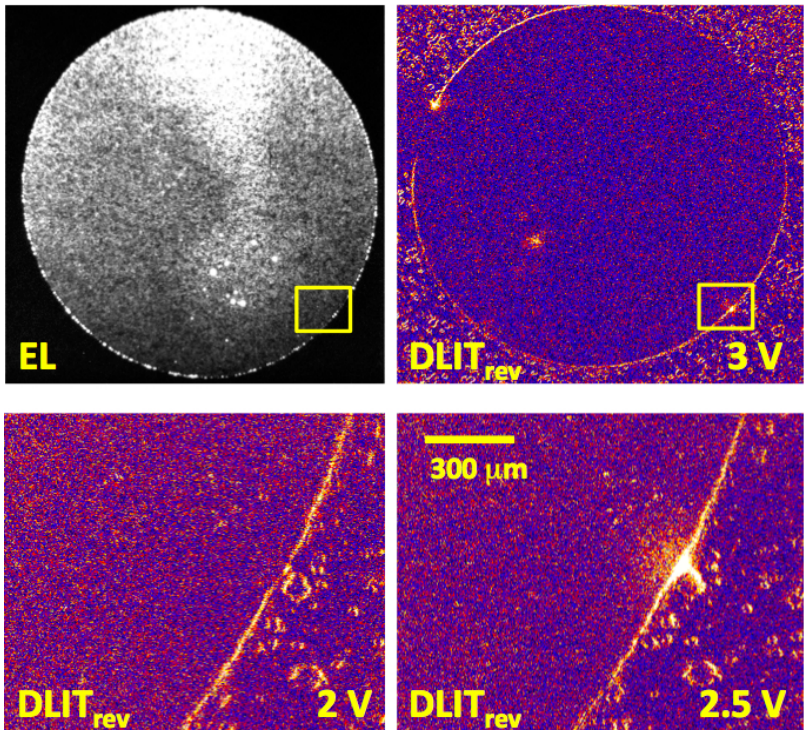

Figure 5.4. EL and reverse-bias DLIT images (top) showing a hot spot in the boxed region that was later investigated by higher-resolution DLIT imaging (bottom). The hot spot appears at 2.5 V reverse bias.

The CdTe edge effects that were specific to EL and appeared at high current densities did not correspond to any specific feature in PL. As shown in the EL image in Fig. 2.15, these edge effects have a different current response than typical uniform luminescence, where they turn on at higher voltage bias but the signal exponentially increases with current. Whereas these features typically surrounded large portions of the perimeter (if not completely), the heat signatures in DLIT that corresponded with the appearance of the EL signatures were few in number. When they did appear, they were more isolated and occur only once or twice in each cell. And the EL edge effects did not always correspond to DLIT hot spots. These DLIT hot spots and EL signatures are most likely the result of poor delineation, with the former being more concentrated or severe and the latter resulting from more than current-crowding. Neither signature is thought to be indicative of a highly detrimental defect with respect to device performance.

5.4. QE, Lifetimes, and Resistive Effects

Tying in quantum efficiency (QE) and lifetime values provides quantitative data. Spatial QE data were acquired through light-beam-induced-current (LBIC) measurements and lifetime values via time-resolved PL (TRPL), as explained in Chapter 4. Side-by-side spatial comparisons were made with EL, PL, and DLIT images and LBIC maps.

The primary difference between data comparisons for CIGS and CdTe was the differences in PL imaging. For CdTe, similar variation in signal and distinct features are seen in EL and LBIC, with the forward-biased LBIC measurements showing more detail corresponding to EL than the unbiased LBIC. This trend also held for CIGS.

EL signal has been shown to be linked to carrier diffusion length in mc-Si solar cells [19] and CIGS samples [7]. In this way, diffusion length is correlated with QE for CdTe. This

inference is made not only because of the similarities between thin-film CIGS and CdTe, but because there is also a large overlap between EL signatures and LBIC maps in CdTe as well as CIGS, particularly for forward-bias LBIC. This comparison in CdTe is shown in Fig. 5.5.

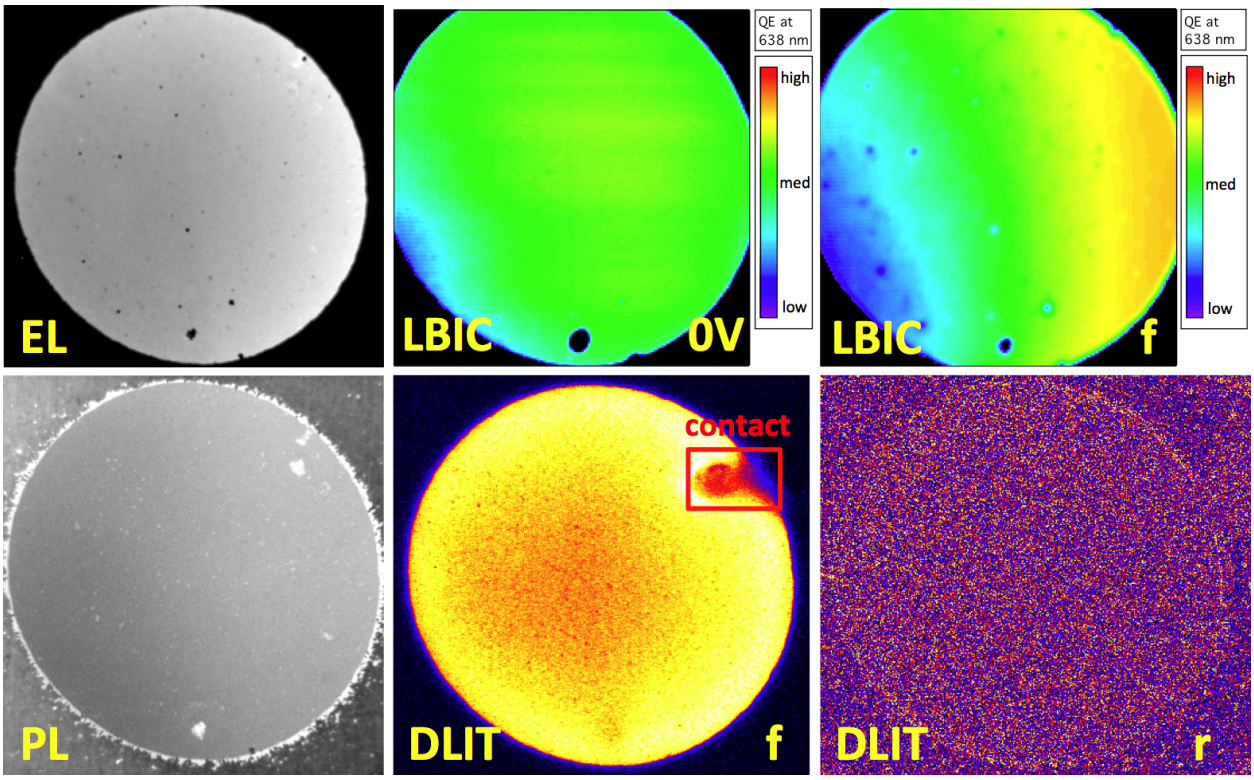

FIGURE 5.5. EL, no bias LBIC, forward-bias LBIC, PL, forward-bias DLIT, and reverse-bias DLIT maps and images of a 9-mm-diameter CdTe sample. There are many overlaps between the EL and LBIC(fwd), some feature similarities in unbiased LBIC and PL, and no distinct hot spots or features in the DLIT images.

The electronics for the LBIC system at CSU, particularly the amplifier, was masking inhomogeneities due to resistance issues for unbiased and reverse-bias LBIC measurements. These resistance effects, which were related to the TCO sheet resistance, were in the top layers of the cell. These variations in sheet resistance were manifested in EL as a decrease in intensity and in forward-bias LBIC as a decrease in QE. These effects limit the extent of these measurements by potentially masking other features located below these areas at different interfaces or in the bulk region. However, many other features are also likely to be seen,

including defects such as delamination or weak-diode effects from an area with insufficient CdS.

The comparison between PL and LBIC for CdTe did not reveal many overlapping features because of the lack of spatial information provided by PL imaging. CIGS, on the other hand, had many feature similarities between EL and PL images that correlated well with LBIC variations, shown in Fig. 5.6, as well as device efficiency and open-circuit collage [7]. The discrepancy between PL and EL for CdTe indicates a limitation of the PL technique. Both techniques depend on material quality and are a function of radiative recombination; therefore it was expected that the data should be more similar than measurements at present.

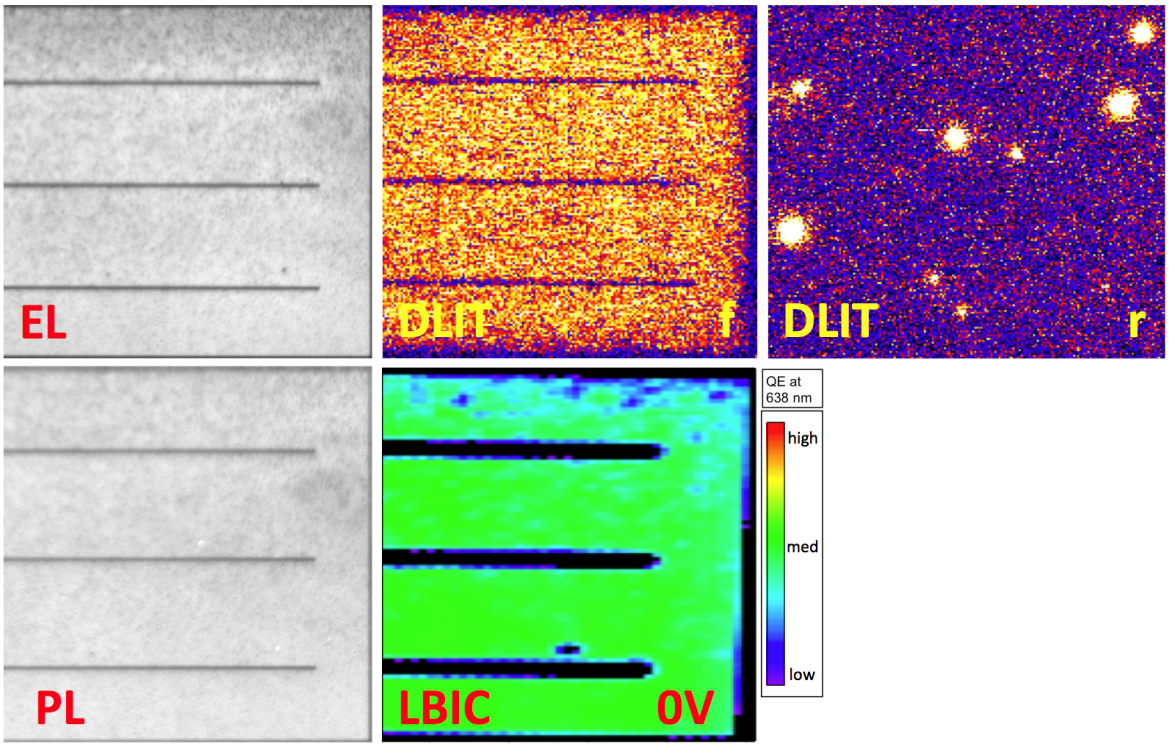

FIGURE 5.6. EL, forward-bias DLIT, reverse-bias DLIT, PL, and unbiased LBIC maps and images of a CIGS device. There are many similar features in EL, and PL, with LBIC variations corresponding well with the aforementioned. DLIT(fwd) is quite uniform, and DLIT(rev) shows many hot spots.

Comparison studies involving minority-carrier lifetime began with the assumption that for CdTe, lifetime and PL is related, since the two have been shown to be highly correlated for both Si and CIGS. The minority-carrier lifetime data on CdTe acquired for this study agreed well with this assumption. Once TRPL measurements were made, the data were compared with average PL signals for each of the measured cells to see if the two correlated. Lifetime was also compared to device parameters. No correlation was found between device efficiency and minority-carrier lifetime. The open-circuit voltage was a better indication of lifetime values. Measurements on CdTe devices show that higher-lifetime material also had a higher PL signal. The same was true for the CdS films that were measured in Chapter 4. The CdS films that were treated with $CdCl_2$ and then annealed at a high temperature had a PL signal that was an order of magnitude higher than the as-deposited films, while lifetimes increased from 2 ns to 3 ns after annealing.

Relationships between resistive effects and luminescence have been found in photovoltaic devices, both Si and thin-film. Data for Si have shown that EL shows similar variations to resistance mapping [19]. An example of mc-Si is shown in Fig. 5.7 that reveals similarities between EL, PL, sheet resistance, and lifetime, but not LBIC. DLIT also shows the presence of hot spots in regions of low luminescence and high sheet resistance.

Studies in correlating thermography signatures to shunts and resistances has also been done on thin-film technologies [28]. Statistical data were gathered from lock-in thermography images, so that shunt variability could be quantified to show that shunt current exhibits a log-normal behavior for CdTe and CIGS (as well as other thin-film technologies). This log-normal behavior was used to determine the effects of the shunt currents on cell efficiency and how shunted cells affected entire module performance.

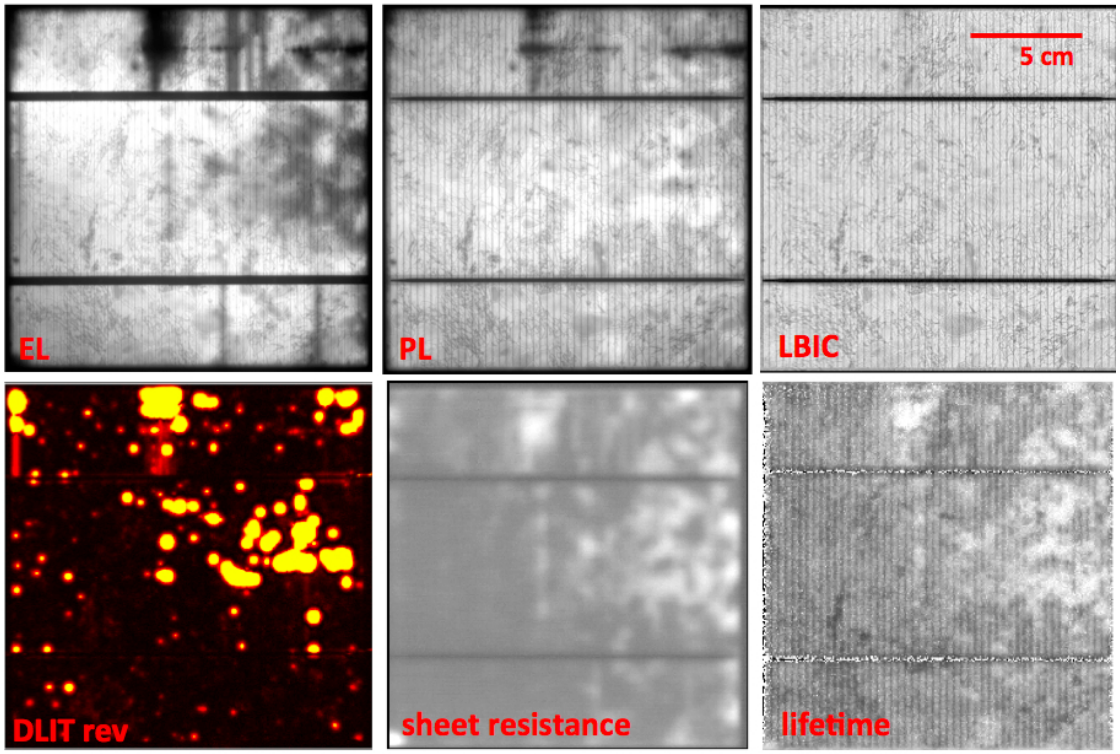

FIGURE 5.7. EL, PL, LBIC, reverse-bias DLIT, sheet resistance, and lifetime maps and images of a multicrystalline Si sample. Brighter regions (yellow in DLIT and white in all others) indicate higher signal. There are dark regions in EL and PL that do not appear in LBIC but show up with hot spots in DLIT, high sheet resistance, and some regions of higher lifetimes.

With regard to series resistance, the lateral series resistance makes quantifying luminescence data complicated, as found in PL imaging studies of silicon wafers [5]. PL studies on Si have also led to the findings that optical properties such as the absorption coefficient can be determined using PL data, which yield more accurate results than using QE data to determine these values [29]. Electronic properties, however, are more easily extracted from QE data rather than from EL [9].

5.5. CONCLUSIONS

Data integration, beginning with EL and PL imaging, device performance parameters, and then adding other spatial characterization measurements helped to construct a more

complete story of the CdTe data. Results previously obtained on Si and CIGS were very useful in determining methods to continue identifying physical causes of defects, particularly shunts.

The integration of data showed that CdTe features and overlaps typically corresponded well with those of CIGS, excluding PL imaging. QE and EL data aligned with one another, particularly when comparing EL images to QE maps obtained with forward-bias LBIC measurements. The unbiased LBIC and reverse-bias maps tended to show fewer features and less overall variations because of the LBIC equipment masking resistive issues otherwise seen at forward bias. Minority-carrier lifetimes extracted from time-resolved PL data show that higher lifetime values correlated with higher PL signal, as seen in PL imaging and spectral PL data. Modeling and data collected on CIGS modules revealed that weak diode and shunted regions affect the local voltage, resulting in changing luminescence as voltage bias changes. This was used when searching for and identifying physical causes of defect areas in luminescence imaging.

CHAPTER 6

Summary and Conclusions

6.1. Establishing Imaging for CdTe

Electroluminescence (EL), photoluminescence (PL), and dark lock-in thermography (DLIT) imaging have been used previously in many photovoltaic materials in order to characterize performance. The work presented here further established these techniques for thin-film CdTe solar cells with the goal of providing rapid spatial characterization of data.

Due to the novel CdTe data acquired with recently-developed imaging techniques, there were many modifications to experimental setups designed for other materials, e.g. Si and CIGS. This work represents one of the first attempt at validating the use of these techniques to characterize CdTe.

The data acquired have assisted in a better understanding of the function of the devices. The imaging techniques, coupled with other spatial measurements, identify inhomogeneities arising from defects and non-uniformities in the materials. The data, however, have not been as definitive as was hoped with respect to identifying specific causes of the image features. Nevertheless, progress has been made to characterize CdTe lab-cell solar cells using these techniques. By integrating imaging data and using data from additional techniques, it is possible to better understand what the image features correspond to in terms of physical defects and abnormalities.

Data collection began with identifying and cataloguing basic luminescence features seen in CdTe images. EL and PL provided spatial information about voltage distribution, current flow, and recombination, while forward- and reverse-bias dark lock-in thermography revealed thermal signatures from current, whether spread out or concentrated because of defects.

Parameterizing the EL and PL data involved extracting the average luminescence intensity, categorizing the cells based on the uniformity of the image, identifying inhomogeneities, determining their size, and comparing signatures across all imaging techniques.

The next step was to identify physical causes and effects of luminescence signatures. This, in turn, aids in identifying the signatures directly related to defects and loss of efficiency. Identifying the causes of the catalogues signatures began with studying the signal intensities as a function of varying operating conditions. The analysis included luminescence intensity profiles acquired from line cuts around features and regions of interest. These profiles were an initial step to quantify the signal. Voltage bias and spectral response of EL signatures were also acquired and analyzed.

6.2. Establishing PL on CdTe

EL proved to be the most useful in revealing device inhomogeneities in CdTe. It was expected that PL would be equally revealing, but features that were identified and catalogued in CdTe cells were less numerous than their EL counterparts. Many of the variations in the TCO layer that appeared in EL were not seen in PL. Moreover, certain EL features such as local decreased luminescence that did appear in PL showed more detail and had higher spatial resolution in the EL images. Part of the difficulty with PL was that it showed more reflection and optical effects, including scattering from the 3-mm-thick glass supersaturate and local bright spots from the glass and TCO.

The use of different filters with PL showed similar spatial variations to each other, but many of the filters transmitted a significant amount of reflected light, as seen by the inhomogeneity of the signal throughout the image and large amount of signal coming from the

area outside of the sample itself. It was difficult therefore to quantify the reflected light or distinguish between luminescence signal and reflected light from the illumination source.

The illumination sources available for the PL measurements were not ideal. The excitation properties of the 630-nm LEDs were not ideal because the light was not monochromatic. Longer wavelengths in the excitation source were not absorbed by the sample and were transmitted to the detector, making it difficult to distinguish PL signal from the reflected light. It was also difficult to get a uniform area of excitation on the stage area. Because of the geometry of the setup, the light sources were directed onto the stage from a slight angle to keep from obstructing the camera. This led to additional internal reflection through the glass substrate and highly scattered light that was transmitted through the angle-dependent filters.

Despite the large amount of reflection, the average PL intensity of fairly uniform devices had a linear response with illumination intensity up to one sun intensity. The signatures that did appear were either optical reflections or correlated with EL signatures (both bright and dark local features). Much like in EL, the features did not vary in size and varied linearly with excitation intensity. PL imaging done on a set of films that had undergone different processing steps showed that PL greatly increased between the CdTe deposition and the $CdCl_2$ and annealing step. The signal rose only slightly after the first copper treatment, decreased after the second copper treatment, and no change was observed after the high-temperature anneal.

6.3. Move Towards the Quantitative

This work has focused on making characterization techniques more useful as inline evaluation tools. Most important are the preliminary attempts to move from qualitative to quantitative information.

EL analysis showed that EL intensity correlated with the open-circuit voltage for CdTe solar cells as expected. Other correlations were found with the fill factor and efficiency, with an even weaker correlation between EL and J_{SC}. For cells that were reasonably uniform, the EL signal response to increasing current was linear. Many of the small to moderate variations seen in the EL images arose from inhomogeneities in the transparent-conductive oxide (TCO) layer. Variance in the conductive TCO affects the lateral sheet resistance, which in turn affects the voltage distribution and EL signal. This was also seen in CIGS with the changing resistivity of the TCO around the front contacts as the voltage bias was increased.

Rough spectral EL data were also acquired through the use of filters to gain insight into what type of emissions contribute to the overall signal. The majority of the EL emission was between 800 and 900 nm. The data implied that the signal drops off by an order of magnitude between 800 and 950 nm. The localized bright EL signatures, including the bright edge effect, had similar spectral dependence as normal luminescence. The interior bright spots and local dark features did not change in size when voltage bias changed. The bright features on the edge, however, had a larger response to changing current. They typically did not begin to appear until current densities near 10 mA/cm^2, and their intensity increased much faster than the regions of normal luminescence.

PL is the most promising technique to achieve quantification, as work has already been done on mcSi to use a series of five PL images to extract performance parameters [21]. Very strong correlations between PL intensity and open-circuit voltage were also found for CIGS [7]. The data taken with the established system did not provide the spatial resolution that was expected. Features in EL and PL did not, for the most part, overlap. Modifications made to the setup, including different illumination sources and filters, did not provide better data.

6.4. Integration of Techniques and Modeling to Identify Defects

By making direct comparisons between imaging data and other characterization techniques, a more comprehensive explanation of inhomogeneities and cell performance was offered for this CdTe study. Despite the lack of overlap between EL and PL for CdTe, there were features and variations seen in forward-bias-DLIT and quantum-efficiency maps acquired from light-beam-induced-current (LBIC) measurements that did correspond with EL signatures. Variations due to resistive effects were reflected in EL and LBIC, with forward-bias LBIC maps showing more variations in signal than their unbiased and reverse-bias counterparts.

Data produced by CIGS modules with relatively wide cells show how the size and severity of certain non-uniformities affect the voltage distribution throughout a cell, and therefore the EL response [9], [10]. While modeling results were compared with experimental EL data acquired on CIGS modules, the techniques were also generalized and applied to lab-size CdTe cells to extract defect and voltage-distribution information.

Defect areas were identified using DLIT, which showed features that displayed characteristics of shunts (hot spots appearing in reverse bias) and weak diodes with low turn-on

voltages (hot spots in forward bias). EL data taken at varying current densities were then used to identify which defects affected different areas at different biases. Line cuts of local dark spots in EL showed that the luminescence in regions directly adjacent to these areas was not decreased. This means that the features of interest in these set of cells did not exhibit shunt-like qualities.

Minority-carrier lifetimes acquired through time-resolved PL measurements were also integrated into the data. As expected, there was a correlation between lifetime and PL. Devices that had higher lifetimes also had higher PL intensities. This was also found for measurements taken on as-deposited and treated CdS films that contained no CdTe.

6.5. Future Work

This work has shown that imaging provides the means of rapidly identifying solar cells with non-uniformity issues related to shunting, resistive effects, and low efficiency. While technique development is in an earlier, more exploratory phase for CdTe compared to other technologies, this work recognizes the potential for imaging techniques applied to thin-film technologies–and the challenge of fully exploiting them.

Much of what has been done with CdTe up to this point is empirical. At this stage of development, imaging techniques provide reasonably informative spatial information for CdTe. The next step is to move beyond correlations to quantify the imaging data. The implementation of EL and PL for CdTe at NREL has helped to pave the way for imaging as a characterization tool, but there is still a considerable amount that can be done with data acquisition and analysis as applied to CdTe.

The limitations for these techniques as applied to CdTe are an important concern. The basis of this work rely on what has been done with CIGS and Si. However, the foundations

of PL measurements on CdTe have significant potential for future development, particularly in acquiring optimal illumination sources. Although no specific method of identification of luminescence features has been established, this further development of imaging techniques, data acquisition, and modeling related to thin-film CdTe PV should continue to be investigated as a powerful characterization tool.

Bibliography

[1] M. A. Green, *Solar Cells: Operating Principles, Technology and System Applications*. Prentice Hall, 1st ed., 1981.

[2] H. Möller, *Semiconductors for Solar Cells*. Artech House, 2nd ed., 1993.

[3] T. Fuyuki, H. Kondo, T. Yamazaki, Y. Takahashi, and Y. Uraoka, "Photographic surveying of minority carrier diffusion length in polycrystalline silicon solar cells by electroluminescence," *Appl. Phys. Lett.*, vol. 86, no. 262108, 2005.

[4] T. Fuyuki, H. Kondo, Y. Kaji, A. Ogane, and Y. Takahashi, "Analytic findings in the electroluminescence characterization of crystalline silicon solar cells," *J. Appl. Phys.*, vol. 101, no. 023711, 2007.

[5] T. Trupke, R. Bardos, M. C. Schubert, and W. Warta, "Photoluminescence imaging of silicon wafers," *Appl. Phys. Lett.*, vol. 89, no. 044107, 2006.

[6] T. Trupke, J. Nyhus, and J. Haunschild, "Luminescence imaging for inline characterization in silicon photovoltaics," *Phys. Status Solidi RRL*, vol. 5, pp. 131–137, 2011.

[7] S. Johnston, T. Unold, I. Repins, A. Kanevce, and K. Zaunbrecher, "Correlations of Cu(In,Ga)Se_2 imaging with device performance, defects, and microstructural properties," *J. Vac. Sci. Technol. A*, vol. 30, no. 04D111, 2012.

[8] U. Rau, "Reciprocity relation between photovoltaic quantum efficiency and electroluminescent emission of solar cells," *Physics Review B*, vol. 76, no. 085303, 2007.

[9] D. Abau-Ras, T. Kirchartz, and U. Rau, *Advanced Characterization Techniques for Thin-film Solar Cells*. (Weinheim, Germany): Wiley VCH Verlag GmbH and Co., 1st ed., 2013.

[10] G. Koishyev, "Analysis of impact of non-uniformities on thin-film solar cells and modules with 2-D simulations," *Colorado State University*, 2010.

[11] X. Wang and M. S. Lundstrom, "On the use of Rau's reciprocity to deduce external radiative efficiency in solar cells," *IEEE J. Photovolt.*, vol. 3, no. 4, 2013.

[12] O. Breitenstein, "Shunt types in crystalline silicon solar cells," *Prog. Photovolt: Res. Appl.*, vol. 12, pp. 529–538, 2004.

[13] K. Zaunbrecher, S. Johnston, and J. Sites, "Non-uniformities in thin-film cadmium telluride solar cells using electroluminescence and photoluminescence," *Proc. 37th IEEE Photovoltaics Specialist Conference*, pp. 002841–002844, 2011.

[14] J. Raguse, J. T. McGoffin, and J. Sites, "Electroluminescence system for analysis of defects in CdTe cells and modules," *Proc. 38th IEEE Photovoltaics Specialist Conference*, pp. 000448–000451, 2012.

[15] M. Topič, "Electroluminescence of thin-film solar cells and photovoltaic modules–calibration aspects," *Proc. 26th European Photovoltaic Specialist Conference*, vol. Hamburg, Germany, 2011.

[16] S. Johnston, F. Yan, D. Dorn, K. Zaunbrecher, M. Al-Jassim, O. Sidelkheir, and K. Ounadjela, "Comparison of photoluminescence imaging on starting multi-crystalline silicon wafers to finished cell performance," *Proc. 38th IEEE Photovoltaics Specialist Conference*, pp. 002161–002166, 2012.

[17] M. Bolkalič, "Spice simulations of circumstances at monolithic contacts of CdTe modules supported by electroluminescence measurements," *Proc. of European Photovoltaic Specialist Conference*, pp. 2222–2225, 2012.

[18] A. Helbig, T. Kirchartz, R. Schaeffler, J. H. Werner, and U. Rau, "Quantitative electroluminescence analysis of resistive losses in CIGS thin-film modules," *Solar Energy Materials & Soar Cells*, vol. 94, pp. 979–984, 2010.

[19] S. Johnston, N. Call, B. Phan, and R. K. Ahrenkiel, "Applications of imaging techniques for solar cells characterization," *Proc. 34th IEEE Photovoltaics Specialist Conference*, pp. 00276–00281, 2009.

[20] A. Kanevce, D. H. Levi, and D. Kuciauskas, "The role of drift, diffusion, and recombination in time-resolved photoluminescence of CdTe solar cells determined through numerical simulation," *Prog. Photovolt: Res. Appl.*, vol. 76, 2013.

[21] C. Shen, H. Kampwerth, and M. Green, "Spatially resolved photoluminescence imaging of essential silicon solar cell parameters," *Proc. 38th IEEE Photovoltaics Specialist Conference*, 2012.

[22] W. K. Metzger, D. Albin, D. Levi, P. Sheldon, X. Li, B. M. Keyes, and R. K. Ahrenkiel, "Time-resolved photoluminescence studies of CdTe solar cells," *J. Appl. Phys.*, vol. 94, no. 3549, 2003.

[23] N. Katz, M. Patterson, K. Zaunbrecher, S. Johnston, and J. Hudgings, "High-resolution imaging of defects in CdTe solar cells using thermoreflectance," *Electronic Letters*, vol. 49, pp. 1559–1561, 2013.

[24] J. F. Hiltner, *Investigation of spatial variations in collection efficiency of solar cells.* PhD thesis, Colorado State University, 2001.

[25] R. M. Geisthardt and J. R. Sites, "Nonuniformity characterization of CdTe solar cells using LBIC," *IEEE Journal of PV*, submitted for publication.

[26] S. Johnston, F. Yan, K. Zaunbrecher, M. Al-Jassim, O. Sidelkheir, and K. Ounadjela, "Quality characterization of silicon bricks using photoluminescence imaging and photoconductive decay," *Proc. 38th IEEE Photovoltaics Specialist Conference*, pp. 000406–000410, 2012.

[27] A. Helbig, T. Kirchartz, R. Schaeffler, J. H. Werner, and U. Rau, "Quantitative electroluminescence analysis of resistive losses in Cu(In,Ga)Se_2 thin-film modules," *Solar Energy Materials & Solar Cells*, vol. 94, pp. 979–984, 2010.

[28] S. Dongaonkar, S. Loser, E. J. Sheets, K. Zaunbrecher, R. Agrawal, T. J. Marksb, and M. A. Alam, "Universal statistics of parasitic shunt formation in solar cells, and its implications for cell to module efficiency gap," *Energy Environ. Sci.*, vol. 6, pp. 782–787, 2013.

[29] E. Daub and P. Wurfel, "Ultralow values of the absorption coefficient of Si obtained from luminescence.," *Phys. Rev. Lett.*, vol. 74, no. 1020, 1995.